NASA TECHNICAL NOTE

NASA TN D-8158

NASA TN D-8158

VIBRATION CHARACTERISTICS OF 1/8-SCALE DYNAMIC MODELS OF THE SPACE-SHUTTLE SOLID-ROCKET BOOSTERS

Sumner A. Leadbetter, Wendell B. Stephens,
John L. Sewall, Joe W. Majka, and Jack R. Barrett

Langley Research Center
Hampton, Va. 23665

NATIONAL AERONAUTICS AND SPACE ADMINISTRATION • WASHINGTON, D. C. • MAY 1976

1. Report No.	2. Government Accession No.	3. Recipient's Catalog No.
NASA TN D-8158		

4. Title and Subtitle
VIBRATION CHARACTERISTICS OF 1/8-SCALE DYNAMIC MODELS OF THE SPACE-SHUTTLE SOLID-ROCKET BOOSTERS

5. Report Date
May 1976

6. Performing Organization Code

7. Author(s)
Sumner A. Leadbetter, Wendell B. Stephens, John L. Sewall, Joe W. Majka, and Jack R. Barrett

8. Performing Organization Report No.
L-10524

9. Performing Organization Name and Address
NASA Langley Research Center
Hampton, Va. 23665

10. Work Unit No.
506-17-25-01

11. Contract or Grant No.

12. Sponsoring Agency Name and Address
National Aeronautics and Space Administration
Washington, D.C. 20546

13. Type of Report and Period Covered
Technical Note

14. Sponsoring Agency Code

15. Supplementary Notes

Jack R. Barrett: Rockwell International.

16. Abstract

Results are reported of vibration tests and analyses of six 1/8-scale models of the space-shuttle solid-rocket boosters. Natural vibration frequencies and mode shapes were obtained for these aluminum-shell models having internal solid-fuel configurations corresponding to launch, midburn (maximum dynamic pressure), and near-endburn (burnout) flight conditions. Test results for longitudinal, torsional, bending, and shell-vibration frequencies are compared with analytical predictions derived from thin-shell theory and from finite-element plate and beam theory. The lowest analytical longitudinal, torsional, bending, and shell-vibration frequencies were within ±10 percent of experimental values. The effects of damping and asymmetric end skirts on natural vibration frequency were also considered. The analytical frequencies of an idealized full-scale space-shuttle solid-rocket-booster structure are computed with and without internal pressure and are compared with the 1/8-scale-model results.

17. Key Words (Suggested by Author(s))
Structural mechanics
Vibrations
Space-shuttle dynamics
Layered shells

18. Distribution Statement
Unclassified – Unlimited

Subject Category 39

19. Security Classif. (of this report)	20. Security Classif. (of this page)	21. No. of Pages	22. Price*
Unclassified	Unclassified	54	$4.25

*For sale by the National Technical Information Service, Springfield, Virginia 22161

VIBRATION CHARACTERISTICS OF 1/8-SCALE DYNAMIC MODELS OF THE SPACE-SHUTTLE SOLID-ROCKET BOOSTERS*

Sumner A. Leadbetter, Wendell B. Stephens, John L. Sewall,
Joe W. Majka, and Jack R. Barrett**
Langley Research Center

SUMMARY

Results are reported of vibration tests and analyses of six 1/8-scale models of the space-shuttle solid-rocket boosters. Natural vibration frequencies and mode shapes were obtained for these aluminum-shell models having internal solid-fuel configurations corresponding to launch, midburn (maximum dynamic pressure), and near-endburn (burnout) flight conditions. Test results for longitudinal, torsional, bending, and shell-vibration frequencies are compared with analytical predictions derived from thin-shell theory and from finite-element plate and beam theory. The lowest analytical longitudinal, torsional, bending, and shell-vibration frequencies were within ±10 percent of experimental values. The effects of damping and asymmetric end skirts on natural vibration frequency were also considered. The analytical frequencies of an idealized full-scale space-shuttle solid-rocket-booster structure are computed with and without internal pressure and are compared with the 1/8-scale-model results.

INTRODUCTION

The structural dynamic characteristics of all launch structures must be predicted and understood during vehicle development and operations. Knowledge of the vibration frequencies, mode shapes, and damping is fundamental to the prevention of aeroelastic and Pogo instabilities and for the prediction of dynamic loads. Analytical methods, normally used to determine these structural dynamic properties, must be verified by experiments to insure their adequacy. Test data, needed to evaluate the analytical methods, are most often obtained from ground-vibration tests of flight-vehicle prototypes and are generally obtained with the expenditure of considerable effort and cost.

*Presented at the 46th Shock and Vibration Symposium, San Diego, California, Oct. 21-23, 1975.

**Rockwell International.

Another and sometimes more expedient method of obtaining experimental data for validating analytical approaches is the use of dynamic scale models as described in references 1 and 2. Specialized vibration models have been used extensively to obtain data on launch vehicles as indicated in references 3 to 7.

The space-shuttle vehicle will have more complex structural dynamic characteristics than previous launch vehicles because four separate, large elements are joined asymmetrically at discrete interfaces. This multielement configuration will have a high modal density in the frequency range of expected dynamic loading, and the dynamic response will have a high degree of directional coupling. Thus, it is important to develop the analytical methods needed to compute accurately frequencies and mode shapes of the various vehicle elements and subsequently to couple these element dynamic properties to predict the total vehicle-response characteristics.

In order to provide a better assessment of analytical modeling capabilities with which to understand the dynamic behavior of shuttle-like configurations, a 1/8-scale dynamic model of an early shuttle-vehicle concept was designed and fabricated for structural dynamics investigations at the Langley Research Center. The 1/8-scale dynamic-model details are described in references 8 to 10.

The complete space-shuttle 1/8-scale dynamic model is shown in figure 1. The assembled model has a simulated lift-off mass of 3975 kg, is 7.43 m long, and consists of four major elements: the orbiter, external tank, and two solid-rocket boosters (referred to herein as SRB). Data from vibration studies of the 1/8-scale model orbiter are reported in references 8 and 11.

The purpose of the present paper is to report the results of vibration studies of the 1/8-scale SRB. Vibration tests of six SRB models containing inert solid fuel are reported and compared with results from analyses based on thin-shell theory and on finite-element plate and beam theory. Additional model studies showing the effects of propellant damping and the addition of end skirts are discussed. Finally, an analytical comparison of the 1/8-scale-model response with that of an idealized full-scale design of the shuttle SRB propellant cylinder with and without internal pressure is presented.

SYMBOLS

A cross-sectional area

E modulus of elasticity

E_p modulus of elasticity of propellant

G	modulus of rigidity in shear
g	acceleration due to gravity
I_x, I_y, I_z	area moments of inertia with respect to roll, pitch, and yaw axes, respectively
I_{xx}	torsional mass moment of inertia
I_{xz}	area product of inertia
J	torsional constant
K	shear factor
k_x, k_y, k_z	linear spring constants along roll, pitch, and yaw axes, respectively
m	number of circumferential nodal circles along a meridan
N_x, N_θ	membrane stress resultants in SRB in axial and circumferential directions, respectively
n	number of full circumferential waves
p	internal pressure
r_i	inner radius of propellant layer
r_r	radius of casing reference surface
t_c	layer thickness of casing
t_p	layer thickness of propellant
$\bar{x}, \bar{y}, \bar{z}$	cross-section centroid eccentricity along roll, pitch, and yaw axes from point of attachment (or model grid point), respectively
$\beta_x, \beta_y, \beta_z$	rotational spring constants along roll, pitch, and yaw axes, respectively
μ	Poisson's ratio

μ_p Poisson's ratio for propellant

ρ mass density

$\bar{\rho}$ effective mass density at casing reference surface

Abbreviations:

FEB finite-element-beam model

FEP finite-element-shell model using plate and/or hexahedral elements

SOR shell-of-revolution model

SRB solid-rocket booster

TEST MODELS AND PROCEDURES

1/8-Scale Models

The design and fabrication of the 1/8-scale SRB (solid-rocket booster) dynamic models are based on an early-vehicle concept (ref. 10) and do not include a significant amount of the structural details. In particular, uniform skin thicknesses are used in lieu of stepped thicknesses or ring reinforced skins. Also, aluminum is used in place of steel for the construction of the major components. Each SRB model consists of three separate parts: a forward skirt, a propellant cylinder, and an aft skirt. A photograph of the SRB model is shown in figure 2.

The scaling relationships between the models and shuttle prototypes are shown in table I. These relationships directly follow from a dimensional analysis of the parameters that control the dynamic behavior of the structure and from the choice of material used in the model. Extrapolating prototype behavior from model test data is accomplished by using these scaling relationships directly. However, the full-scale design of the shuttle SRB flight hardware approved for fabrication is significantly different from the structural concept upon which the 1/8-scale-model design is based. For example, the model SRB consists of one continuous cylindrical section, a forward skirt, and an aft skirt; whereas the flight-hardware prototype consists of an aft propellant segment, including engine section, six propellant sections, a forward skirt, and a nose cone. Also, the 1/8-scale-model dimensions are based on an overall length of 45.72 m and a diameter of 3.96 m as compared with the length of 43.94 m (excluding the engine nozzle) and a diameter of 3.70 m called for in the planned flight prototype.

In this study a comprehensive assessment was made of the propellant-cylinder dynamic response. More limited data were gathered on propellant cylinders with end skirts attached.

Model Description

The assembled 1/8-scale model includes a forward skirt, a propellant cylinder, and an aft skirt as shown in figure 2. The end skirts, the casing of the propellant cylinder, and the attachment end rings are all constructed of aluminum. As indicated in table I, the aluminum component thicknesses of the model are three times the nominal smeared steel thicknesses of the prototype components so that stiffnesses and masses can be properly proportioned. The forward skirt is a short cylinder which is 0.495 m in diameter and 0.533 m in length. The basic skin thickness of the forward skirt is 0.102 cm and has local reinforcement in the region of the external-tank connection. Details of local reinforcements and attachment frames are given in reference 10. The aft skirt consists of a short cylindrical section and a larger conical section, each with a nominal skin thickness of 0.157 cm. The cylindrical section is attached to the propellant cylinder and is 0.113 m long. The conical section is 0.551 m long and flares to an outer diameter of 0.775 m. Details of local reinforcement and attachment frames are given in reference 10.

End rings used for the attachment of the forward and aft skirts to the propellant cylinders are shown in figure 2. Fastening of the SRB elements to other 1/8-scale-model elements is achieved through the skirt structures.

The propellant cylinder is composed of an outer aluminum casing, an inert interior solid cylindrical propellant layer, and two end frames for attachment to the end skirts. Six 1/8-scale propellant cylinders were fabricated and tested. Two propellant cylinders were used to simulate each of the flight conditions, that is, lift-off, approximate maximum dynamic pressure (midburn), and near endburn (burnout). The cylinder casings are 0.476 cm thick, 3.73 m long, and have an outer diameter of 0.495 m. The length of the simulated propellant layer is 3.69 m which allows for a propellant recess of 2.0 cm from each edge. The length of the propellant cylinder is 3.74 m since each attachment ring extends 0.005 m past the casing edge. The propellant-layer thicknesses are 0.173 m, 0.0897 m, and 0.0198 m for the lift-off, midburn, and burnout flight conditions, respectively. End views of each of the cylinders for the various flight conditions are shown in figure 3. The masses of the various SRB componènts are given in table II.

The solid propellant is a viscoelastic material whose elastic properties are characterized by dynamic moduli defined as complex quantities that vary with frequency, temperature, and strain level. The simulated propellant used for the 1/8-scale dynamic model was inert UTI-610 manufactured by the United Technology Center (UTC) Division of United Aircraft Corporation. The simulant consists of essentially the same binder-

fuel-curative components as the UTP-3001 propellant used in the Titan launch vehicle. Inert sodium chloride and inert ammonium sulphate were substituted for the ammonium perchlorate in the inert UTI-610.

The particular batch of UTI-610 that was used in the 1/8-scale model yielded samples having a density of 4.407 kg/m^3. Estimates of the elastic moduli of the propellant were provided by the manufacturer (ref. 10) and were based on a low strain level of approximately 10^{-6}. Measurements of moduli based on moderate-to-high strains of 0.005 to 0.05 using specimens of the same propellant material are reported in reference 12. Both sets of material properties are listed in table III. The large differences in moduli are consistent with those due to high and low strain observed in reference 13 for propellant materials similar to that used in the 1/8-scale SRB. These large differences suggest that the propellant properties deserve careful attention, particularly with regard to the strain environment. Other factors such as strain rate, frequency, temperature, and aging may also have large effects on the propellant modulus. An in-house series of low-to-moderate strain-level tests on a specimen taken from one of the models indicated better agreement with the low moduli values of reference 12. Therefore, the studies presented are based on the low moduli values of reference 12 unless otherwise noted.

Suspension System

The tests were conducted to determine the lower natural frequencies and mode shapes of an SRB model in an unrestrained condition. To simulate free-free boundary-restraint conditions for the experimental study, the SRB model was supported in a horizontal position as shown in figures 2 and 4, and as discussed in reference 14. Steel cables and rope slings were used to support the model and were located near the node lines of the mode being studied. For the tests to determine the first longitudinal and torsional responses, the cables were located near the model midlength and small elastic cables were attached to the skirt attachment rings (see fig. 4) to stabilize the test configuration statically. The vibration exciters were suspended with separate steel cables and were attached to the model as needed to excite the modes of interest. For torsional response two exciters were required as shown in figure 4.

Data Acquisition and Reduction

The instrumentation for the SRB vibration studies provided continuous electronic signals that were a measure of the dynamic response of the model to the sinusoidal input force. The data-acquisition system provided a means for monitoring exciter inputs and accelerometer and force-gage output signals and for performing on-site data analyses. Transducers used during the test program included piezoelectric accelerometers and force gages that were attached to the test article by means of either a mechanical fastener

or a movable vacuum mount. The movable accelerometers were used primarily to obtain detailed mode shapes and shell-response data. Electromagnetic exciters were used to vibrate the model at discrete frequencies to obtain modal-response data.

A schematic layout of the data-acquisition system is given in figure 5. The accelerometer and force-gage output signals were indicated on meters and plotted by an $x - y_1, y_2$ recorder in the form of amplitude and phase components referenced to the input force signal. The servo-oscillator indicated in figure 5 was used to control the exciter force level. The data were analyzed to obtain the required modal-response information by means of either the so-called co-quad method, discussed in references 15 and 16, or the Kennedy-Pancu or phase-plane method discussed in references 17, 18, and 19. Structural damping coefficients were determined from the power-off decrement, the coincident response, or from the phase-plane diagram.

Typical data for a test article representing the midburn flight condition are shown in figures 6 and 7. A single electrodynamic exciter, oriented such that a constant sinusoidal force could be applied in the pitch direction, was located at one end of the cylinder. The output from an accelerometer located at the other end of the cylinder provided the response signal. In figure 6 the out-of-phase (referred to as quadrature or quad) and in-phase (referred to as coincident or co) components of the output acceleration with respect to the input force are shown for a limited frequency range. As shown in references 15 and 16, the modal amplitude and frequency can be determined from the quadrature peak value, whereas a measure of the damping can be obtained from the coincident component. In figure 7, for the same test data the quadrature component and the frequency are plotted as a function of the coincident component of the acceleration referred to the force. As shown in reference 17, an indication of modal purity, modal amplitude, frequency, and damping can be obtained from these data.

The data in figures 6 and 7 exemplify uncoupled (labeled "first bending") and coupled (labeled "second bending") response conditions of a 1/8-scale SRB model. The first-bending mode occurred at a frequency well separated from other modes, whereas the second-bending mode occurred at a frequency near the model first torsion mode and a shell mode. These coupled modes could be adequately separated in the laboratory by the use of appropriate test methods: namely, by adjusting the suspension system as well as the location and direction of the vibration exciters.

ANALYTICAL MODELS

Analysis Approach

The 1/8-scale SRB model is complicated by thick-shell effects; that is, transverse shear deformation and motion between the aluminum casing and the propellant simulant.

In addition, the SRB structure is not symmetrical since end skirts are reinforced for attachment to the rest of the shuttle system. In order to account for these effects properly in the 1/8-scale models and in the comparative full-scale SRB configuration, analyses were performed with three types of analytical models: a finite-element-plate model, a finite-element-beam model, and a shell-of-revolution model.

Flat-plate elements were used for the finite-element-plate model (FEP) to represent the casing, and hexahedral elements were used to represent the thick propellant layer present at midburn and lift-off flight conditions. This model also is capable of accounting for the asymmetries of the end skirts as well as external tank-attachment supports. The ability of this model to predict accurately the SRB response is of interest, since this class of models is a candidate for use in full-scale shuttle-tankage analysis. Inherent in this dynamic model are many degrees of freedom which can be reduced for computational efficiency by the application of a Guyan reduction technique and by taking advantage of axial planes of symmetry, which exist in the propellant cylinder of the 1/8-scale SRB. The application of the FEP analysis was limited to the propellant cylinder and did not include the asymmetric end skirts.

A more computationally efficient finite-element model was used to study the effects of asymmetrically attached end skirts and damping and the overall agreement with test data for the membrane (longitudinal and torsional) and bending modes. This simpler model uses linear-beam elements to represent the casing and propellant and is referred to as the finite-element-beam (FEB) model. It is computationally more efficient than the previous model but cannot be used to calculate general shell modes involving distortion of the cylinder cross section.

A shell-of-revolution (denoted herein by SOR) analysis based on thin-shell theory was used when analytical data were needed to show shell-response trends such as the effect of high internal pressure on shell response at SRB burnout. This method is the most computationally efficient of the three analytical approaches. However, circumferential structural asymmetries, transverse shear deformations, and thick-shell effects are either approximated or ignored in this approach.

The finite-element models are based on the displacement formulation of the NASTRAN code (ref. 20), and the shell-of-revolution code (ref. 21) is based on a numerical integration technique.

Finite-Element-Shell Model

In order to simplify the finite-element model with plate and/or hexahedral elements (referred to herein as FEP), the forward and aft skirts are not included. Therefore, the length of the cylinder model is the same as that of the casing. The SRB was originally modeled for an earlier NASTRAN vibration study (ref. 10), and this model has been modi-

fied for use in the present study. The relatively coarse grid used in reference 10 was satisfactory since only the lower mode responses are of interest, and shell responses higher than two circumferential waves (n = 2) and three axial half-waves (m = 3) generally yield frequencies above the range of interest. By use of axial symmetry planes, only a one-quarter (90^{o}) model of the SRB propellant cylinder with proper combinations of symmetric, antisymmetric, and antisymmetric-symmetric boundary conditions along the longitudinal edges is required. This reduces the number of degrees of freedom by a factor of almost four and the total run time by a factor of three. Thus, the basic grid for the FEP analysis is a 3×12 rectangular mesh which allows a rectangular element size spanning 30^{o} circumferentially and 1/12th of the propellant-cylinder length axially.

The casing is modeled by using the NASTRAN isotropic flat-plate element CQUAD2, and the propellant layer for the midburn and lift-off flight conditions is modeled by using the NASTRAN isotropic solid hexahedron element CHEXA1. The propellant thickness is modeled by two and three equal-thickness layers for the midburn and lift-off flight conditions, respectively, by using the CHEXA1 element. The propellant layer at burnout is thin enough for a single layer of CQUAD2 elements to be used to represent its behavior. The beam element CBAR is used to represent the ring frames at the forward and aft edges of the cylinder. The CQUAD2 and CBAR elements include both membrane and bending stiffnesses. The CQUAD2 node motion is described by three displacements and two inplane rotational degrees of freedom. The constant-strain CHEXA1 element is described by three displacements at each node. A preliminary study showed that a Guyan reduction equivalent to seven equally spaced longitudinal stations yielded well-converged results. The number of degrees of freedom for the lift-off, midburn, and burnout models is 253, 211, and 71, respectively, for symmetry-symmetry axial boundary conditions and is slightly higher for the asymmetry-asymmetry and asymmetry-symmetry boundary conditions.

The accuracy of this 90^{o} model with the Guyan reduction is shown in table IV for the casing without the interior propellant layer for the relevant response modes. The converged solutions were obtained by using a shell-of-revolution code. The data show that longitudinal, torsional, and bending behavior are quite accurately predicted for the first several modes of response. The shell-response predictions ($n \geqq 2$) degenerate rapidly, however, as the axial-mode number increases. The first two frequencies at these circumferential wave numbers are of acceptable accuracy if it is recalled that the propellant is not included and that the stiffer models which have the propellant layer included were found to be more accurate. Comparisons at burnout, midburn, and lift-off flight conditions are made in subsequent sections of this report.

The propellant is an incompressible material with a Poisson's ratio that approaches a value of 0.5. This value will cause the stress-strain matrix for the NASTRAN solid element, CHEXA1, to become singular since terms are present which contain the factor

$(1 - 2\mu)$ in the denominator. Even with μ_p equal to 0.49, the stresses are overly magnified and the element, consequently, becomes overly stiff. For the FEP model, therefore, μ_p was taken to be 0.4 to avoid possible numerical instabilities for μ_p near 0.5. The effect of varying μ_p is considered further subsequently.

Finite-Element-Beam Model

The finite-element-beam model (FEB) was used to investigate the transverse shear and damping effects of the propellant mass as well as the effect of the forward and aft skirts on the frequencies. This FEB model can be used to investigate only the longitudinal, torsional, and bending modes of the SRB test model. The length of the FEB model was the same as that of the propellant cylinder, that is, 3.74 m.

The propellant cylinder was modeled as two six-element beams of equal length. One beam represents the casing and the other beam represents the propellant. Two beam elements of equal length were used to model the forward skirt. These beam elements were offset from the shell neutral surface to account for the asymmetric character of the stiffening in the forward skirt. The aft-skirt cylinder is modeled as one beam element and the aft-skirt cone is modeled by two equal length elements. The cross-sectional and mass properties are given in tables V and VI, respectively. These tables include data required for modeling the lift-off, midburn, and burnout flight conditions.

The two beams representing the casing and the propellant can either be rigidly connected at common grid points or by springs to allow relative motion between the two beams. The rigidly attached model results (without end skirts) were verified by excellent agreement with elementary beam theory (ref. 22) for longitudinal and torsional frequencies as shown in table VII. Results by the FEB analysis for the bending response are slightly lower than those based on beam theory because the beam shear effect is accounted for in the element formulation.

The mass-distribution matrix was generated in this analysis by using the coupled mass matrix formulation described in reference 23. The number of degrees of freedom retained for this model was 84 without end skirts and 114 with skirts.

Shell-of-Revolution Model

The simplest and most computationally efficient manner of calculating frequencies for this study is to use a one-dimensional shell-of-revolution code. Since the thin-shell criterion of the theory is violated in the midburn and lift-off flight-condition studies, some caution must be used in interpreting the results for cases in which propellant-stiffness contribution exceeds the magnitude for the casing stiffness. For the cases studied this occurred only for the lift-off shell modes ($n \geq 2$). Also, the total mass of the thick propellant layer must be accounted for by using an effective mass density $\bar{\rho}$ defined by

$$2\pi\bar{\rho}r_r t_p = \pi\rho\left[\left(r_r - \frac{t_c}{2}\right)^2 - \left(r_r - \frac{t_c}{2} - t_p\right)^2\right]$$

Here, r_r is the radius of the reference surface located at the casing midsurface, ρ is the mass density of the propellant, and t_c and t_p are the layer thicknesses of the casing and propellant, respectively.

Model details such as the different lengths of the propellant layer and the casing can be easily and accurately modeled by using the shell-of-revolution approach. However, shear deformations and circumferential asymmetries in the shell could not be accounted for by using this approach. Therefore, the asymmetrically stiffened end skirts are not analyzed by using this model. For the SOR model, the casing length is taken to be 3.73 m and extends 2.0 cm past each end of the propellant layer. The end frames are attached 1.27 cm from each edge of the casing. The elastic and cross-sectional properties of the discretely modeled end frames are given in table VIII.

RESULTS AND DISCUSSION

General

The results are presented as four main topics. First, experimental data for the propellant cylinders are presented. Second, a comparison of these results is made with the various analytical models. Third, the influence of propellant damping, addition of end skirts, and variation of propellant materials on shell response are presented. Fourth, a brief study of the effect of internal pressure on the 1/8-scale SRB and on the full-scale shell dynamic response is presented. Unless otherwise specified, all discussions refer to SRB models without the end skirts, and the moduli of the propellant used are based on the values given in reference 12.

Test Results for the SRB 1/8-Scale Model

The frequencies and structural damping coefficients obtained experimentally for the six 1/8-scale propellant cylinders at the three flight conditions and with free-free boundary conditions are presented in table IX. Two SRB scale models are tested at each flight condition and are identified by numbers 1 to 6. The responses excited are characterized as longitudinal and torsional membrane modes (n = 0), bending modes (n = 1), and general shell modes ($n \geq 2$) which involve distortion of the cylinder cross section. The n-number identifies the number of full harmonic circumferential waves, and the m-number identifies the number of nodal circles occurring along a longitudinal generatrix which is analogous to the number of axial half-waves for a freely supported shell. For the free-free cylinders rigid-body modes in each direction are present but are ignored in the presentation of

results. Higher longitudinal modes could not be excited. Modes involving a local motion of the propellant layer were found in the 200 Hz range for the lift-off and midburn flight conditions. Also, there were some shell modes ($n \geqq 2$) which could not be identified due to the close coupling of modes and the resulting modal interference. These modes were ignored since their behavior could not be determined over the length of the models. In general, frequencies higher than about 250 Hz were not considered.

Comparison of Test and Analysis

In order to demonstrate the effect of the propellant modulus on the stiffness of the shell, a longitudinal frequency and a general shell ($n = 2$) frequency at the lift-off flight condition are compared in figure 8 with the results of an analysis in which the propellant-stiffness contribution is ignored. For the longitudinal response the membrane stiffness of the propellant is negligible compared with the casing stiffness, and very little error is introduced if the propellant modulus is in error. For the shell mode, however, the contribution of the propellant bending stiffness is larger than that of the casing bending stiffness, and variations in the modulus of the propellant directly affect the accuracy of the analysis. This effect should be less pronounced as the propellant-layer stiffness contribution becomes less than that of the casing, that is, as the burnout condition is approached.

Shell-of-revolution results.- A comparison of the experimental data with the SOR model analysis is presented first since the 1/8-scale SRB propellant cylinders are rotationally symmetric and since all modes of response can be accounted for by this analytical procedure. The longitudinal mode frequencies for the three flight conditions as a function of axial mode number m are shown in figure 9 for both the experimental data and the SOR analysis. The experimental results for these models are denoted by the symbols and correspond to the average of the frequencies obtained at the various modal responses of a particular flight condition. At the midburn and lift-off flight conditions, the analysis overestimates the frequency because transverse shear effects were neglected. The agreement becomes much better as the propellant mass becomes progressively less, that is, approaches burnout. The error varies from 15 percent at lift-off to less than 1 percent at burnout.

The analytical torsion-mode frequencies for the three flight conditions along with available experimental data are linear functions of the axial mode number as shown in figure 10. Excellent agreement with experimental data is obtained for the burnout flight condition, but transverse shear effects cause the analytical prediction to differ as much as 15 percent at lift-off.

The bending mode ($n = 1$) frequencies are shown in figure 11, and, again, frequencies are essentially linear functions of axial mode number. The agreement between experi-

ment and analysis is quite good in all cases for $m = 2$ and 3 (i.e., first and second bending modes), and for $m = 4$ the agreement is within 10 percent.

The general shell modes are presented in figures 12 to 14 as functions of circumferential wave number for the lift-off, midburn, and burnout flight conditions. The shell-response frequencies ($n \geq 2$) decrease with decreasing mass. This result occurs because the bending stiffness of the propellant is equal to or greater than the bending stiffness of the casing. Thus, the propellant stiffness decreases as the cube of the propellant-layer thickness, whereas the mass decreases only as a linear function of the thickness. This is quite the opposite of the situation shown in figures 9 to 11 where the membrane stiffness remains nearly constant for all flight conditions because the casing membrane stiffness is much larger than the propellant-membrane stiffness. In these cases, the increase in frequency as mass decreases is due to the mass loss.

There are no experimental data for comparison with analysis in figure 12 for the shell responses at lift-off, but the trend of the analytical behavior indicates that $n = 2$ is the minimum-frequency shell mode. (The $n = 1$ results are for bending modes and not for shell modes.) The agreement between analysis and experiment is good except for the higher m values in the $n = 2$ and $n = 3$ modes of the midburn case (fig. 13). For these modes analysis and experiment differ by as much as 33 percent with analysis underestimating the frequency. This discrepancy for the shell modes ($n \geq 2$) of the midburn flight condition suggests that the error is due to a low estimate of the propellant modulus, since the agreement between analysis and experiment is excellent for the burnout flight condition (fig. 14) where the propellant stiffness is small compared with the casing stiffness.

A typical set of mode shapes for normal displacements is shown in figure 15 for the first six modes at $n = 2$ for the burnout flight condition. The straight lines indicate the profile of an undeformed SRB meridian, and the mode shape is superimposed on this meridian. The circular symbols on the undeformed meridian denote the ring-attachment locations.

First longitudinal, torsional, bending, and shell modes at $n = 2$ are compared in figure 16 for the three flight conditions with the available experimental data. The increase in longitudinal, torsional, and bending frequencies is due primarily to a decrease in the mass of the propellant layer. For the shell modes, however, the propellant layer contributes a significant portion of the total bending stiffness at lift-off, and the decrease in response frequency is attributed to the decrease in propellant stiffness. Thus, at lift-off the bending mode is the lowest and at burnout the general shell mode is the lowest. Shell modes greater than $n = 2$ do not yield minimum frequencies, as shown previously in figures 12 to 14.

Finite-element-plate results.- A further comparison of experimental and analytical results is shown in figures 17 and 18 by using the finite-element-plate (FEP) model. The analytical results based on the NASTRAN FEP model are presented and compared with both the SOR analysis and the experimental data for various flight conditions. The frequencies for both the bending and shell modes are shown as a function of axial mode number in figures 17 and 18. In figure 17 the FEP analysis gives excellent agreement with experiment for the three flight conditions. The first two bending frequencies are within 5 percent of the experimental values. The agreement between the analyses and experiment for the first three axial modes at burnout and midburn in figure 18 is no worse than 17 percent. At lift-off the agreement between the analyses was particularly good but no experimental data were obtained.

The FEP model yielded modes which could not be defined in terms of n- and m-numbers in the 200 Hz region of response for the lift-off and midburn flight conditions. These modes involved a local motion of the propellant layer and were high enough not to be of interest in this investigation.

Table X shows that the FEP model accurately predicts the membrane (longitudinal and torsional) and bending (n = 1) frequencies in the lower range of axial mode numbers. In general, the FEP models have yielded results for all modes of response and flight conditions that differ from the expected results by as much as 16 percent but usually differ by only 5 percent.

Finite-element-beam results.- Also shown in table X are the results from the NASTRAN finite-element-beam (FEB) analysis along with the previously discussed SOR results. The separate beam elements of the case and propellant may be attached either rigidly or by springs at common node points. For the results presented in table X the elements are attached rigidly. The agreement of the FEB model with experiment is generally good, although the analytical longitudinal frequency is 17 percent in error at lift-off and the error for higher bending frequencies tends to grow. These analytical errors can be corrected by adding spring stiffnesses for all six degrees of freedom. It was hypothesized in reference 13 that the propellant shears with respect to the casing (with the bondline still maintained). This behavior was modeled by the introduction of springs. The stiffnesses of the springs were first estimated by static structural analyses and then adjusted by a simple curve-fitting procedure, based on an acceptable agreement between test and analytical frequencies, to establish an approximate model. Table XI shows the final stiffnesses used in the analytical models for the three flight conditions, and table XII summarizes the analytical results of the spring-beam-element model. The agreement with experimental data for the beam model with springs is 10 percent or better. The remaining comparisons in this report for the beam model (FEB) are based on the inclusion of springs.

Additional Model Studies

Damping results.- Theoretical and experimental results for models that consider damping effects in the propellant cylinders are summarized in tables XIII and XIV. Experimental structural damping coefficients in table XIV are highest for the first longitudinal mode (0.17), which helps to explain why this mode was difficult to excite and the higher longitudinal modes could not be found. Damping coefficients in torsion and bending are significantly lower (0.008 to 0.08) and more typical of all-metal structures.

Because the propellant is a viscoelastic material, its elastic moduli are complex quantities representing the inherently combined elastic and material damping properties. By referring to reference 12 the dynamic modulus may be defined as

$$E_p = E'_p + iE''_p$$

where the real quantity E'_p is the storage modulus and the imaginary quantity E''_p is the loss modulus. This expression may also be written as

$$E_p = E'_p\left(1 + i\,\frac{E''_p}{E'_p}\right)$$

where E''_p/E'_p is a loss factor or loss tangent which, from reference 13, can be shown to be equal to the material structural damping coefficient. The shear moduli and shear damping properties can be described similarly. In the present analytical studies, these effects were simulated in the NASTRAN beam model by including the propellant structural damping coefficient with the storage modulus E'_p in the material property input data and then by solving for the eigenvalues of the resulting complex frequency equation by using NASTRAN's Rigid Format 7. This is essentially the same approach as that used in reference 13 for a NASTRAN SRB model made up of contiguous ring elements. The frequencies and structural damping coefficients given in tables XIII and XIV, respectively, were obtained for a loss factor of 0.5; the frequencies in table XIII come from the imaginary parts and the structural damping coefficients in table XIV come from the real parts of the complex eigenvalues. As shown in table XIII the agreement of analysis with experiment is good, and the changes from the FEB frequencies given in table XII are slight for the cases studied. Also, the change in frequency due to the different propellant moduli amounts to no more than a 3 percent difference for the cases studied. In table XIV it is shown that the agreement between theory and experiment for structural damping coefficients is poor for the bending modes but is reasonably good for the membrane modes. The analysis predicts the damping trends for both bending and membrane modes. The undamped frequencies for these beam and membrane modes have been shown previously to be only slightly affected by the propellant modulus.

SRB skirt results.- The FEB model was also used to compare the analytical and experimental frequencies of the SRB with forward and aft skirts attached for the three flight stages. Table XV summarizes the results of this study and shows the agreement for the lift-off and midburn frequencies to be within 5 percent (except for the third bending mode at midburn). Experimentally determined structural damping coefficients are also presented in this table. Experimental data for the burnout flight-condition model with skirts are not available for comparison. On examining the results, the analysis showed that the torsion mode and second beam bending mode are strongly coupled for the midburn and lift-off flight conditions. A comparison of tables XII and XV shows that the addition of the skirts lowers the lift-off and midburn frequencies and the burnout membrane frequencies by approximately 10 percent, whereas burnout bending frequencies may be lowered by as much as 25 percent.

Elastic-property-variation results.- Two problems related to the modeling of the propellant material have been noted in this report. One problem is related to the wide variation in the elastic modulus which is apparently a function of strain level and frequency. The other problem is related to numerical singularities which occur as a result of using solid finite elements that are based on a displacement formulation to model incompressible materials. The former problem is expected to affect only the shell modes since the total membrane stiffness is derived almost entirely from the casing stiffness. The effect on the shell frequencies of using the higher modulus values of reference 10 rather than the lower modulus values of reference 12 for the lift-off and burnout flight conditions is shown in figures 19(a) and 19(b) where comparisons are made by using the SOR models. The curves indicate that the lower modes (i.e., the lower m values) are influenced the most and that frequencies are increased by as much as 125 percent and 29 percent for the lift-off and burnout cases, respectively.

The variation in natural-frequency response with changes in Poisson's ratio for the FEP analysis is shown in figure 20 for the first shell mode at $n = 2$ of the lift-off flight condition. The bargraph shows relatively wide variations in frequency for values of Poisson's ratio above about 0.4. The changes due to values higher than 0.4 are suspected to be due to numerical singularities induced in the NASTRAN solid element as Poisson's ratio approaches 0.5. The value of 0.4 for Poisson's ratio was selected in the present report to avoid such numerical instabilities when the CHEXA1 solid elements were used in the FEP models.

Comparison With Idealized Full-Scale Behavior

Some appreciation of the differences between the behavior of the scale model and the full-scale model can be determined by studying analytically the behavior of the full-scale model at the burnout flight condition. An SOR analysis is used to obtain the frequencies and mode shapes of an idealized full-scale SRB without skirts or bulkheads. The

geometric and material properties used are given in table XVI. The SRB is composed of six equal-length propellant-cylinder segments and a motor-case skirt. Each of the propellant cylinders is 4.06 m long. The motor-case skirt is composed of four cylindrical segments which are 2.18, 3.04, 3.04, and 0.50 m long, respectively. The 2.18 m segment attaches to the aft propellant cylinder, and the 0.50 m segment is the aft component of the motor-case skirt.

The six propellant segments and the four segments of the motor-case skirt are all cylinders. Asymmetries in the structure are neglected for the analysis. The 10 cylindrical segments are connected by joint rings with the elastic properties shown in table XVII. Such a joint ring is also placed at the forward edge of the model. At the aft edge of the motor case, the aft skirt ring (referred to in table XVII) is used. The two 3.04 m segments of the motor-case skirt are each reinforced at one-third points along the meridian with the motor-case ring. Finally, the support ring is located in the 2.18 m segment of the motor-case skirt at a distance of 0.495 m from the motor-case skirt juncture to the aft propellant cylinder. For modeling purposes this large support ring is divided into two equal parts located 0.343 m and 0.648 m from the propellant cylinder and motor-case skirt juncture.

The membrane and bending frequencies are shown in figure 21 as a function of axial mode number, and the shell mode frequencies are shown in figure 22 as a function of circumferential wave number for the burnout flight condition. Also shown in figure 21 with dashed lines are frequencies at which the SRB is subjected to a static-pressure loading that is present during combustion of the propellant. A simple membrane stress state was assumed that neglects ring loads and rotations and assumes the stress resultants to be given by

$$N_x = \frac{pr_i^2}{2r_r}$$

$$N_\theta = pr_i$$

where r_i is the inner radius of the propellant and r_r is the radius of the casing reference surface. The applied pressure p is 4.02 MPa. The responses shown in figure 21 are essentially unaffected by the static pressure.

The results in figure 21 are similar in character to those in figures 9 to 11 except that the free-vibration frequencies for first longitudinal and torsional modes are lower by a factor of about 9.5 and the bending-mode response is lower by a factor of 11.

Additional results in figure 22 show the influence of the large internal pressure expected at burnout on shell frequency for both the 1/8-scale and full-scale models. The ordinate axes in figure 22 are at an 8:1 ratio for comparison purposes. The shell frequencies are affected significantly and the static stress state increases the lower axial-mode burnout frequencies by at least a factor of 2.5. The free-vibration frequencies of the full-scale model show a behavior similar to that of the 1/8-scale model, but the frequencies are lower by a factor of about 13. Deviation of the full-scale free-vibration results from the scaled results based on a scale factor of 8 are attributed primarily to differences in the full-scale structural designs. Thus, direct scaling comparisons cannot be made for free vibrations. For frequencies with static pressure added, however, the response ratio closely approximates the 8:1 factor.

Typical mode shapes for the $n = 2$ frequencies are shown in figure 23 (at $p = 0$). The straight lines indicate the profile of the undeformed SRB meridian, and the mode shape is superimposed on this meridian. The circular symbols on the undeformed meridian denote ring locations.

CONCLUDING REMARKS

Vibration characteristics of six 1/8-scale solid-rocket-booster dynamic models have been determined both experimentally and analytically. Two models were used to represent each of three flight conditions corresponding to lift-off, midburn, and burnout conditions. Frequencies have been determined for these SRB propellant-cylinder models with and without end skirts, and structural damping coefficients have been presented for the propellant cylinder at the lift-off flight condition.

The study showed that the finite-element shell model composed of flat-plate elements could be used to calculate frequency responses to within 3 percent of experimental data for the lowest membrane and bending modes and to within 6 percent for the lower shell modes. However, discrepancies with experiment as large as 33 percent were noted for the higher shell modes and were attributed to the relatively coarse grid used in the finite-element analyses. Also, the NASTRAN three-dimensional element used in some of the analyses cannot account for material incompressibility, and a value of Poisson's ratio less than the measured material values for the propellant was used to avoid singularities in the stiffness matrix. A value of Poisson's ratio equal to 0.4 was found to be sufficient to avoid the stiffness singularity occurring at a value of 0.5. Wide variations in the propellant-layer modulus due to frequency and strain level cause difficulty in assessing the accuracy of the various models for thick propellant layers.

A finite-element-beam model was used to assess the effects of end skirts and damping. The addition of end skirts does not appreciably affect the correlation of the experi-

mental and analytical results and lowers the frequency of membrane and bending modes by no more than 10 percent. The effect of damping on analytical frequencies is small, and reasonably accurate structural damping coefficients for torsional and longitudinal responses were calculated. The high damping present in the first longitudinal response mode accounts for the inability to find the higher longitudinal natural frequencies experimentally.

A shell-of-revolution analysis was effectively used to determine the effects of changes in propellant-layer thickness and internal pressure on dynamic response even though the thin-shell criterion for this analysis is violated. The shell-of-revolution analysis gave good agreement with all vibration modes in the near-burnout propellant condition. For thicker propellant conditions, beam and torsional mode agreement was good, but agreement for the shell modes was only fair at higher frequencies.

Analytical comparisons were made between the behavior of an idealized full-scale shuttle SRB (solid-rocket booster) and that of scale models in the near-burnout condition. Results show that full-scale models exhibit similar trends in behavior, but results cannot be directly compared to scale models due to significant differences in the full-scale structural designs. The effects of internal pressure on both the scale model and the full-scale model are shown to be small or negligible for bending and for longitudinal and torsional modes. The internal pressure, however, raised the shell frequencies significantly.

The present study was intended to provide early data on vibrations of space-shuttle-like solid-fuel tanks. Experimental results suggest that, in tests of unpressurized tankage, some difficulty may be experienced in separating shell modes from bending modes in near-burnout fuel conditions. Significant damping is likely to be observed only in the longitudinal vibration modes. Analytical results suggest that elementary finite-element-beam models and finite-element-plate models can be used effectively to predict membrane, bending, and lower shell modes. For higher shell modes, more refined finite-element or shell-of-revolution analyses will be required.

Langley Research Center
National Aeronautics and Space Administration
Hampton, Va. 23665
March 22, 1976

REFERENCES

1. Runyan, H. L.; Morgan, H. G.; and Mixson, J. S.: Use of Dynamic Models in Launch-Vehicle Development. AGARD Rep. 479, May 1964.

2. Guyett, P. R.: The Use of Flexible Models in Aerospace Engineering. Tech. Rep. No. 66335, Brit. R.A.E., Nov. 1966.

3. Mixson, John S.; and Catherine, John J.: Comparison of Experimental Vibration Characteristics Obtained From a 1/5-Scale Model and From a Full-Scale Saturn SA-1. NASA TN D-2215, 1964.

4. Jaszlics, Ivan J.; and Morosow, George: Dynamic Testing of a 20% Scale Model of the Titan III. AIAA Symposium on Structural Dynamics and Aeroelasticity, Aug.-Sept. 1965, pp. 477-485.

5. Leadbetter, S. A.; and Raney, J. P.: Model Studies of the Dynamics of Launch Vehicles. J. Spacecraft & Rockets, vol. 3, no. 6, June 1966, pp. 936-938.

6. Pinson, Larry D.; and Leonard, H. Wayne: Longitudinal Vibration Characteristics of 1/10-Scale Apollo/Saturn V Replica Model. NASA TN D-5159, 1969.

7. Grimes, P. J.; McTigue, L. D.; Riley, G. F.; and Tilden, D. I.: Advancements in Structural Dynamic Technology Resulting From Saturn V Programs. Volume II. NASA CR-1540, 1970.

8. Mason, P. W.; Harris, H. G.; Zalesak, J.; and Bernstein, M.: Analytical and Experimental Investigation of a 1/8-Scale Dynamic Model of the Shuttle Orbiter.
   Volume I – Summary Report. NASA CR-132488, 1974.
   Volume II – Technical Report. NASA CR-132489, 1974.
   Volume IIIA – Supporting Data. NASA CR-132490, 1974.
   Volume IIIB – Supporting Data. NASA CR-132491, 1974.

9. Bernstein, M.; Coppolino, R.; Zalesak, J.; and Mason, P. W.: Development of Technology for Fluid-Structure Interaction Modeling of a 1/8-Scale Dynamic Model of the Shuttle External Tank (ET). NASA CR-132549, 1974.
   Volume I: Technical Report.
   Volume II: Supporting Data – Appendixes A Through C.

10. Levy, A.; Zalesak, J.; Bernstein, M.; and Mason, P. W.: Development of Technology for Modeling of a 1/8-Scale Dynamic Model of the Shuttle Solid Rocket Booster (SRB). NASA CR-132492, 1974.

11. Pinson, Larry D., Coordinator: Analytical and Experimental Vibration Studies of a 1/8-Scale Shuttle Orbiter. NASA TN D-7964, 1975.

12. Hufferd, William L.: Measured Properties of Propellant for Solid Rocket Booster of One-Eighth Scale Dynamic Shuttle Model. NASA CR-144938, 1976.

13. Dynamic Characterization of Solid Rockets. Rep. No. 73W-00271 (Contract No. NAS8-14000), Federal Systems Div., IBM Corp., Sept. 1973. (Available as NASA CR-144189.)

14. Herr, Robert W.: Some Cable Suspension Systems and Their Effects on the Flexural Frequencies of Slender Aerospace Structures. NASA TN D-7693, 1974.

15. Keller, Anton C.: Vector Component Techniques: A Modern Way To Measure Modes. Sound & Vib., vol. 3, no. 3, Mar. 1969, pp. 18-26.

16. Salyer, Robert A.; Jung, Ed J., Jr.; Huggins, Stacy L.; and Stephens, Barry L.: An Automatic Data System for Vibration Modal Tuning and Evaluation. NASA TN D-7945, 1975.

17. Schoenster, James A.: Measured and Calculated Vibration Properties of Ring-Stiffened Honeycomb Cylinders. NASA TN D-6090, 1971.

18. Schoenster, James A.; and Taylor, Nancy L.: A Sinusoidal-Vibration Analysis Program for Experimental Data. NASA TM X-2789, 1973.

19. Turner, Lloyd J., Jr.: An Analytical Investigation of a Vector Technique for Determining Normal Mode Amplitudes From Vibration Data. M.S. Thesis, Virginia Polytech. Inst., 1968.

20. McCormick, Caleb W., ed.: The NASTRAN User's Manual (Level 15). NASA SP-222(01), 1972.

21. Cohen, Gerald A.: User Document for Computer Programs for Ring-Stiffened Shells of Revolution. NASA CR-2086, 1973.

22. Den Hartog, J. P.: Mechanical Vibrations. Second ed., McGraw-Hill Book Co., Inc., 1940.

23. MacNeal, Richard H., ed.: The NASTRAN Theoretical Manual (Level 15). NASA SP-221(01), 1972.

TABLE I.- PERTINENT SCALING RELATIONS FOR 1/8-SCALE MODEL OF SRB

[Subscripts: f denotes full-scale prototype; m denotes scaled model]

Physical quantity	Magnitude of –	
	Propellant	Structure[a]
Length (overall) or displacement, L	$8L_m = L_f$	$8L_m = L_f$
Mass density	$\rho_m = \rho_f$	$3\rho_m = \rho_f$
Modulus of elasticity	$E_m = E_f$	$3E_m = E_f$
Area	$8^2A_m = A_f$	$8^2A_m = 3A_f$
Area moment of inertia, I	$8^4I_m = I_f$	$8^4I_m = 3I_f$
Volume, V	$8^3V_m = V_f$	$8^3V_m = 3V_f$
Weight	$8^3\rho_m V_m = \rho_f V_f$	$8^3\rho_m V_m = \rho_f V_f$
Longitudinal stiffness	$8^2E_mA_m = E_fA_f$	$8^2E_mA_m = E_fA_f$
Bending stiffness	$8^4E_mI_m = E_fI_f$	$8^4E_mI_m = E_fI_f$
Frequency, f	$f_m = 8f_f$	$f_m = 8f_f$

[a]Aluminum used in model to represent steel in the prototype.

TABLE II.- MASS OF COMPONENTS OF 1/8-SCALE SRB MODEL

Component	Mass, kg
Casing	76.02
Propellant, lift-off	1065.86
Propellant, midburn	698.40
Propellant, burnout	171.00
Forward ring	1.50
Aft ring	1.09
Forward skirt	6.58
Aft skirt	14.86

TABLE III.- MATERIAL PROPERTIES OF 1/8-SCALE SRB MODEL

Property	Casing	Propellant[a] (ref. 10)	Propellant[a] (ref. 12)
E, MPa	72 394.0	172.4	30.0
ρ, kg/m^3	7.164	4.407	4.407
μ	0.3	0.5	0.5

[a]Properties selected at a nominal room temperature of 22° C and a frequency range of 100 to 120 Hz.

TABLE IV.- CONVERGENCE STUDY FOR FREQUENCIES OF 1/8-SCALE ALUMINUM CASING OF FEP MODEL COMPARED WITH SOR ANALYSIS

Mode			Frequency, Hz		Error, percent
Type	n	m	SOR	FEP	
1st longitudinal	0	1	661.9	663.7	0.3
2d longitudinal	0	2	1312.8	1335.7	1.7
3d longitudinal	0	3	1931.9	2008.2	3.9
1st torsional	0	1	410.3	397.5	-3.1
2d torsional	0	2	820.7	804.4	-2.0
3d torsional	0	3	1231.5	1222.1	-.8
1st bending	1	2	195.8	206.3	5.4
2d bending	1	3	465.8	486.5	4.4
Shell	2	0	58.4	65.2	11.6
Shell	2	1	87.6	107.4	22.6
Shell	2	2	126.6	161.3	27.4
Shell	2	3	207.7	266.1	28.1
Shell	3	0	146.5	157.5	7.5
Shell	3	1	159.0	189.2	19.0
Shell	3	2	195.3	265.3	35.8
Shell	3	3	255.0	368.0	44.3
Shell	4	0	279.3	297.8	6.6
Shell	4	1	283.6	315.9	11.4
Shell	4	2	295.5	364.0	23.2
Shell	4	3	319.7	448.4	71.3

TABLE V.- CROSS-SECTIONAL PROPERTIES FOR ELEMENTS USED IN NASTRAN FEB MODEL OF SRB WITH SKIRTS ATTACHED

Property	Casing elements	Propellant elements			Forward-skirt elements		Aft-skirt elements		
		Lift-off	Midburn	Burnout	Inner	Outer	Cylinder	Core, inner	Core, outer
Area, cm^2 . . .	73.39	1 523.80	1 111.48	272.13	23.68	19.87	24.41	36.01	43.83
I_z, cm^4	22 077	271 162	229 547	74 378	5 011	5 003	7 442	12 942	24 563
I_y, cm^4	22 077	271 162	229 547	74 378	9 103	6 701	7 442	16 256	30 374
J, cm^4	44 154	542 308	459 095	148 757	15 026	11 672	14 884	29 207	54 934
$\bar{y}$, cm					7.99	4.92			
K	0.5	0.9	0.52	0.5	0.5	0.5	0.5	0.8	0.8

TABLE VI.- PROPERTIES OF DISCRETE MASS AND TORSIONAL MASS MOMENTS OF INERTIA OF NASTRAN FEB MODEL OF 1/8-SCALE SRB WITH SKIRTS ATTACHED

Grid-point position	I_{xx}, g-m^2	Mass, kg	I_{xx}, g-m^2		
			Lift-off	Midburn	Burnout
Casing, forward edge	1.244	0.00394			
Casing, aft edge	1.171	0.00280			
Casing interior points	1.972				
Propellant, forward edge			7.153	5.791	1.877
Propellant, aft edge			7.153	5.791	1.877
Propellant, interior points			14.920	12.610	4.087
Forward skirt, outer edge	0.282	0.00399			
Forward skirt, interior point	0.206	0.00064			
Forward skirt, attachment	0.389	0.00486			
Aft skirt, attachment	0.372	0.00726			
Aft skirt, cylinder-cone edge	0.681	0.00726			
Aft skirt, cone interior point	0.811	0.00086			
Aft skirt, outer edge	1.364	0.00604			

TABLE VII.- COMPARISON OF FEB MODEL FREQUENCIES WITH THEORY

$[E_p = 172.4 \text{ MPa}; \quad \mu_p = 0.50]$

Mode			Frequency at lift-off, Hz		Frequency at midburn, Hz		Frequency at burnout, Hz	
Type	n	m	FEB	Ref. 22	FEB	Ref. 22	FEB	Ref. 22
1st longitudinal	0	1	181.4	181.4	215.15	215.47	376.45	379.80
1st torsional	0	1	146.3	148.0	156.15	155.89	238.14	239.0
1st bending	1	2	56.13	59.03	66.26	71.25	117.17	127.17

TABLE VIII.- RING ELASTIC AND CROSS-SECTIONAL PROPERTIES USED IN SOR ANALYSIS OF 1/8-SCALE SRB MODEL

Property	Forward ring	Aft ring
E, GPa	72.394	72.394
A, cm^2	3.258	2.426
I_x, cm^4	1.973	1.428
I_z, cm^4	1.819	1.274
I_{xz}, cm^4	-0.982	0.753
GJ, $GN-m^2$	20.06	6.74
$\bar{x}$, cm	1.024	1.120
$\bar{z}$, cm	0.975	0.871

TABLE IX.- EXPERIMENTAL FREQUENCIES AND STRUCTURAL DAMPING COEFFICIENTS OF PROPELLANT CYLINDERS FOR 1/8-SCALE SRB MODEL WITH FREE-FREE BOUNDARY CONDITIONS

Mode			Frequency at burnout, Hz		Structural damping coefficient at burnout		Frequency at midburn, Hz		Structural damping coefficient at midburn		Frequency at lift-off, Hz		Structural damping coefficient at lift-off	
Type	n	m	Model 1	Model 2	Model 1	Model 2	Model 3	Model 4	Model 3	Model 4	Model 5	Model 6	Model 5	Model 6
1st longitudinal	0	1	373.4	369.5	0.017	0.027	187.5	185.9	0.127	0.154	149.7	156.6	0.174	0.166
1st torsional	0	1	237.2	235.5	.023	.013	147.5	145.5	.050	.040	135.3	135.1	.056	.068
1st bending	1	2	112.6	112.2	.005	.005	64.6	64.8	.008	.009	54.1	54.2	.009	.008
2d bending	1	3	265.6	263.4	.004	.012	150.2	150.9	.033	.037	126.5	126.6	.027	.026
3d bending	1	4		435.3			240.0	241.7	.064	.095	201.8	204.8	.078	.066
Shell	2	1	54.7	52.9	.013	.033								
Shell	2	2	77.6	75.6	.032	.019	103.0	114.7						
Shell	2	3	121.7	120.0	.032	.013	131.0							
Shell	2	4	196.7	195.4	.014	.012								
Shell	2	5	297.0	290.5	.016	.012	200.0	194.4						
Shell	2	6						247.5						
Shell	3	5	230.2	227.0	.045									
Shell	4	5	268.0											

TABLE X.- FREQUENCIES FOR THREE ANALYSES AND TESTS FOR MEMBRANE AND BENDING MODES FOR THREE FLIGHT CONDITIONS

Mode			Test frequency, Hz		Analysis frequency, Hz		
Type	n	m			FEP	FEB (rigid)	SOR
(a) Lift-off							
			Model 5	Model 6			
1st longitudinal	0	1	149.7	156.6	128.7	177.4	175.3
1st torsional	0	1	135.3	135.1	131.6	144.8	155.7
1st bending	1	2	54.1	54.2	56.8	55.3	54.4
2d bending	1	3	126.5	126.6	126.1	134.0	130.7
3d bending	1	4	201.8	204.8	177.3	227.9	216.6
(b) Midburn							
			Model 3	Model 4			
1st longitudinal	0	1	187.5	185.9	178.0	211.2	214.2
1st torsional	0	1	147.5	144.5	145.0	154.2	158.9
1st bending	1	2	64.6	64.8	69.8	65.3	66.4
2d bending	1	3	150.2	150.9	153.9	158.3	157.8
3d bending	1	4	240.0	241.7		268.6	262.3
(c) Burnout							
			Model 1	Model 2			
1st longitudinal	0	1	373.4	369.5	366.9	375.5	369.4
1st torsional	0	1	237.2	235.5	227.9	237.6	237.5
1st bending	1	2	112.6	112.2	115.9	116.2	111.8
2d bending	1	3	265.6	263.4	272.5	282.0	264.6

TABLE XI.- SPRING STIFFNESSES AT ELEMENT NODES FOR NASTRAN FEB MODEL OF 1/8-SCALE SRB PROPELLANT CYLINDERS

Spring constant	Lift-off	Midburn	Burnout
k_x, GN/m	0.377	0.516	6.031
k_y,k_z, GN/m	0.613	0.533	0.296
β_x, kN-m	20.999	27.070	163.097
β_y,β_z, kN-m	7.744	26.638	329.696

TABLE XII.- PROPELLANT-CYLINDER TEST COMPARISONS WITH FEB MODELS WITH AND WITHOUT SPRINGS

Mode			Test frequency, Hz		FEB model frequency, Hz	
Type	n	m			Rigid	With springs
(a) Lift-off						
			Model 5	Model 6		
1st longitudinal	0	1	149.7	156.6	177.4	143.2
1st torsional	0	1	135.3	135.1	144.8	132.1
1st bending	1	2	54.1	54.2	55.3	54.5
2d bending	1	3	126.5	126.6	134.0	121.8
3d bending	1	4	201.8	204.8	227.9	183.7
(b) Midburn						
			Model 3	Model 4		
1st longitudinal	0	1	187.5	185.9	211.2	183.0
1st torsional	0	1	147.5	145.5	154.2	144.5
1st bending	1	2	64.6	64.8	65.3	65.9
2d bending	1	3	150.2	150.9	158.3	149.2
3d bending	1	4	240.0	241.7	268.6	229.9
(c) Burnout						
			Model 1	Model 2		
1st longitudinal	0	1	373.4	369.5	375.5	371.8
1st torsional	0	1	237.2	235.5	237.6	235.6
1st bending	1	2	112.6	112.2	116.2	115.0
2d bending	1	3	265.6	263.4	282.0	261.5

TABLE XIII.- COMPARISON OF EXPERIMENTAL AND ANALYTICAL FREQUENCIES AT LIFT-OFF OF 1/8-SCALE SRB PROPELLANT CYLINDER WITH STRUCTURAL DAMPING ADDED

Mode			Experimental frequency, Hz		Frequency for FEB,[a] Hz	
Type	n	m	Model 5	Model 6	Ref. [b]10	Ref. [b]12
1st longitudinal	0	1	149.7	156.6	152.7	147.4
1st torsional	0	1	135.3	135.1	135.9	134.2
1st bending	1	2	54.1	54.2	55.6	54.7
2d bending	1	3	126.5	126.6	127.1	123.8
3d bending	1	4	201.8	204.8	197.2	189.3

[a]Loss factor, 0.5.

[b]See table III for material properties of propellant.

TABLE XIV.- COMPARISON OF EXPERIMENTAL AND ANALYTICAL STRUCTURAL DAMPING COEFFICIENTS AT LIFT-OFF FOR 1/8-SCALE SRB PROPELLANT CYLINDER

Mode			Experimental structural damping coefficient		Analytical structural damping coefficient for FEB[a]	
Type	n	m	Model 5	Model 6	Ref. [b]10	Ref. [b]12
1st longitudinal	0	1	0.174	0.166	0.180	0.160
1st torsional	0	1	.056	.068	.083	.070
1st bending	1	2	.009	.008	.030	.020
2d bending	1	3	.027	.026	.090	.080
3d bending	1	4	.078	.066	.168	.161

[a]Loss factor, 0.5.

[b]See table III for material properties of propellant.

TABLE XV.- COMPARISON OF EXPERIMENTAL AND ANALYTICAL FREQUENCIES OF 1/8-SCALE SRB MODEL WITH END SKIRTS ATTACHED

Mode			Experimental frequency, Hz	Experimental structural damping coefficient	Frequency for FEB with skirts, Hz
Type	n	m			
(a) Lift-off					
			Model 5 with skirts		
1st longitudinal	0	1	143.4	-----	142.1
1st torsional	0	1	129.7	0.055	128.2
1st bending	1	2	50.7	.010	51.5
2d bending	1	3	117.3	.021	115.1
3d bending	1	4	186.6	.043	177.7
(b) Midburn					
			Model 4 with skirts		
1st longitudinal	0	1	-----	-----	180.2
1st torsional	0	1	139.8	0.034	[a]139.4
1st bending	1	2	59.3	.007	60.7
2d bending	1	3	135.2	.023	137.8
3d bending	1	4	160.2	.062	214.7
(c) Burnout					
1st longitudinal	0	1			341.8
1st torsional	0	1			[a]212.0
1st bending	1	2			93.0
2d bending	1	3			210.0

[a]Strongly coupled with closest bending mode.

TABLE XVI.- MATERIAL AND GEOMETRIC PROPERTIES OF FULL-SCALE SRB MODEL WITHOUT SKIRTS

Property	Casing	Propellant
E, MPa	199 955.0	30.0
μ	0.3	0.5
ρ, kg/m^3	20.27	4.407
Length, m	33.16	------
Radius (outer), m	1.85	1.84
Radius (inner), m	1.84	1.69

TABLE XVII.- RING PROPERTIES FOR FULL-SCALE SRB MODEL WITHOUT SKIRTS

Type	A, cm^2	I_x, cm^4	I_z, cm^4	I_{xz}, cm^4	J, cm^4	$\bar{x}$, cm	$\bar{z}$, cm
Joint ring	17.48	39.25	161.83	8.16	4.25	-0.165	0.536
Motor-case ring	18.00	819.98	34.55	15.61	1.91	10.795	3.800
Aft-skirt ring	110.45	14 277.56	934.44	-287.32	138.19	9.357	6.764
Support ring, forward	15.73	847.45	72.38	122.33	1.47	13.360	-0.874
Support ring, aft	15.73	847.45	72.38	-122.33	1.47	13.360	0.874

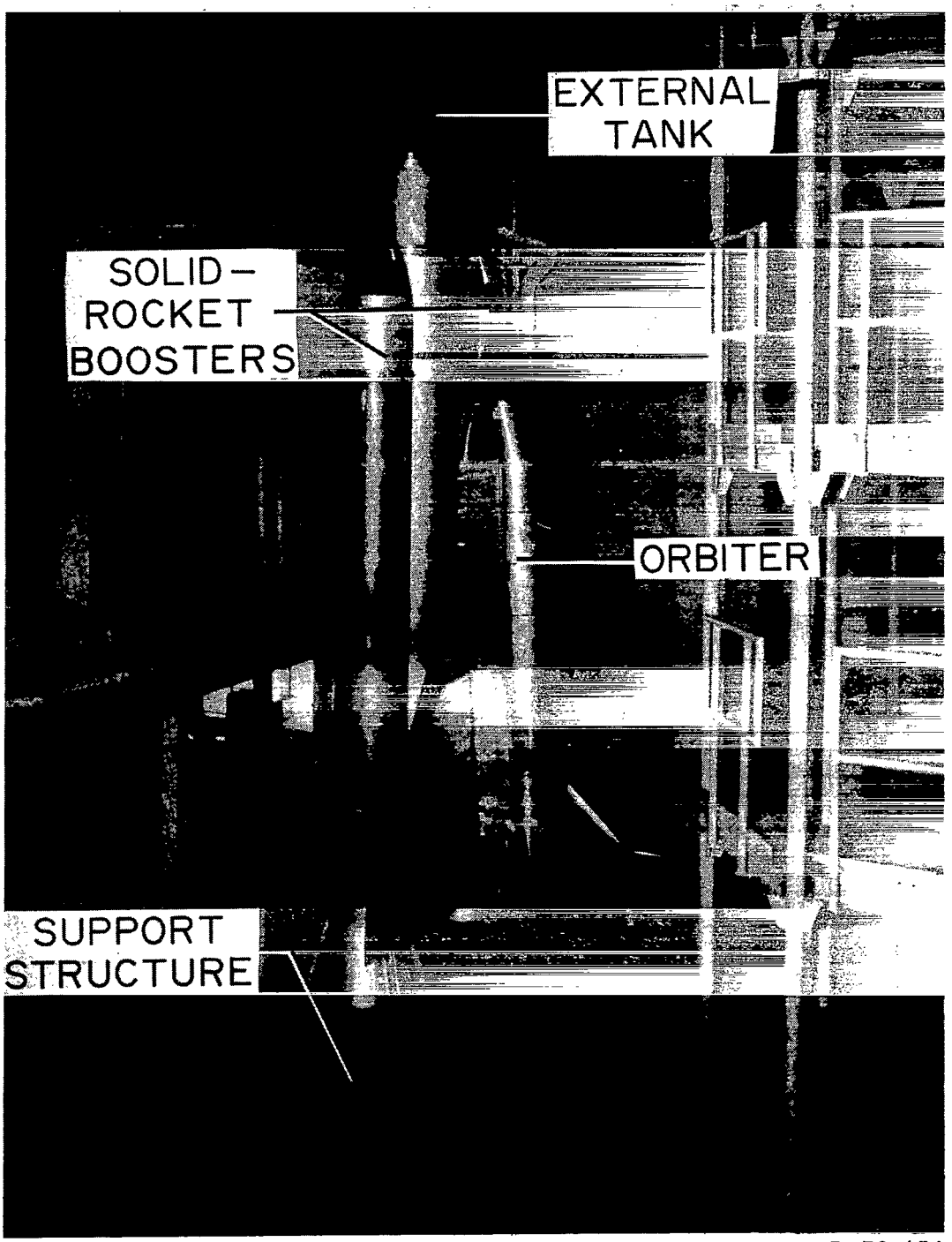

L-76-154

Figure 1.- Space-shuttle 1/8-scale dynamic model.

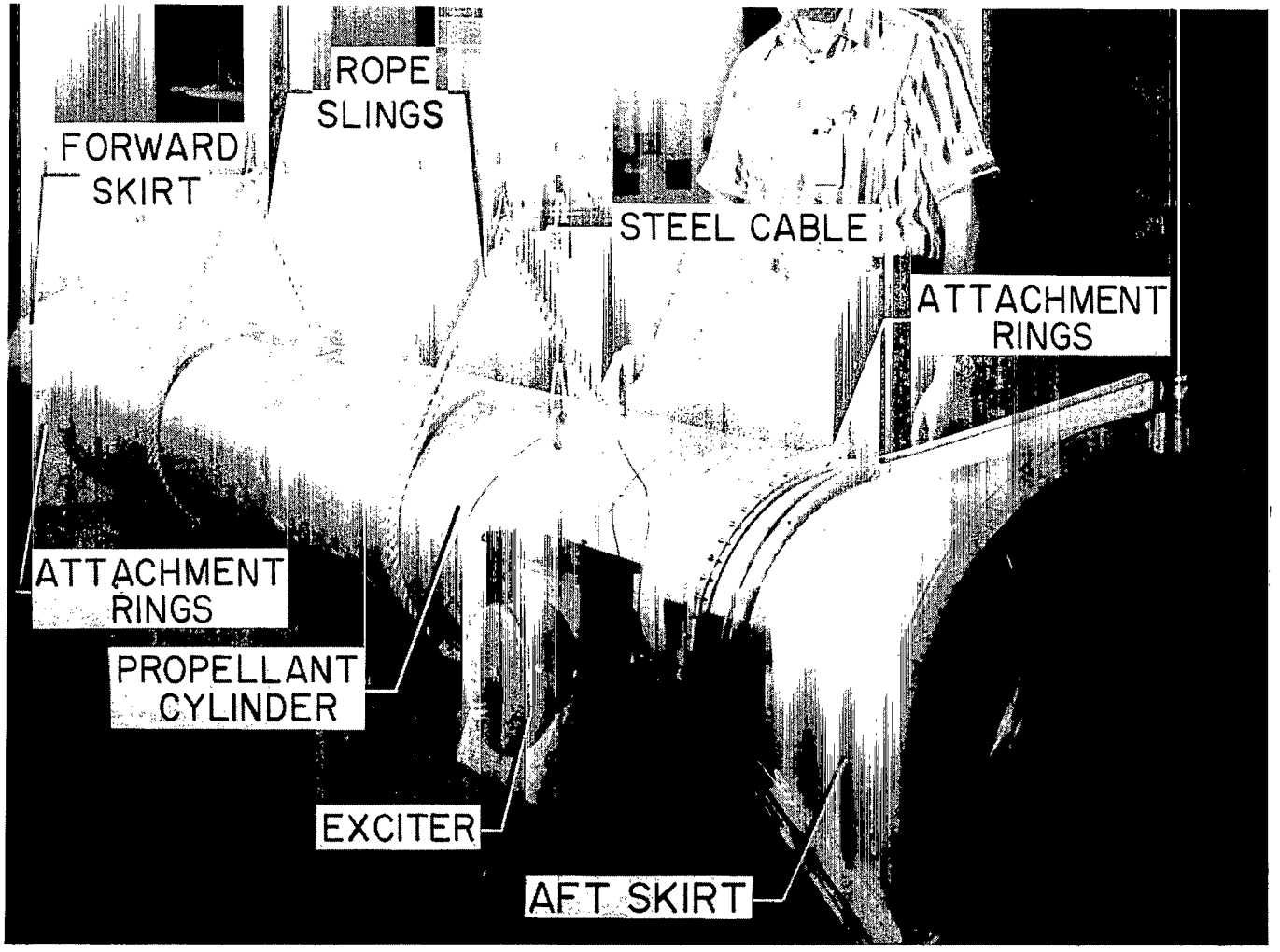

L-76-155

Figure 2.- A 1/8-scale dynamic model of the solid-rocket booster.

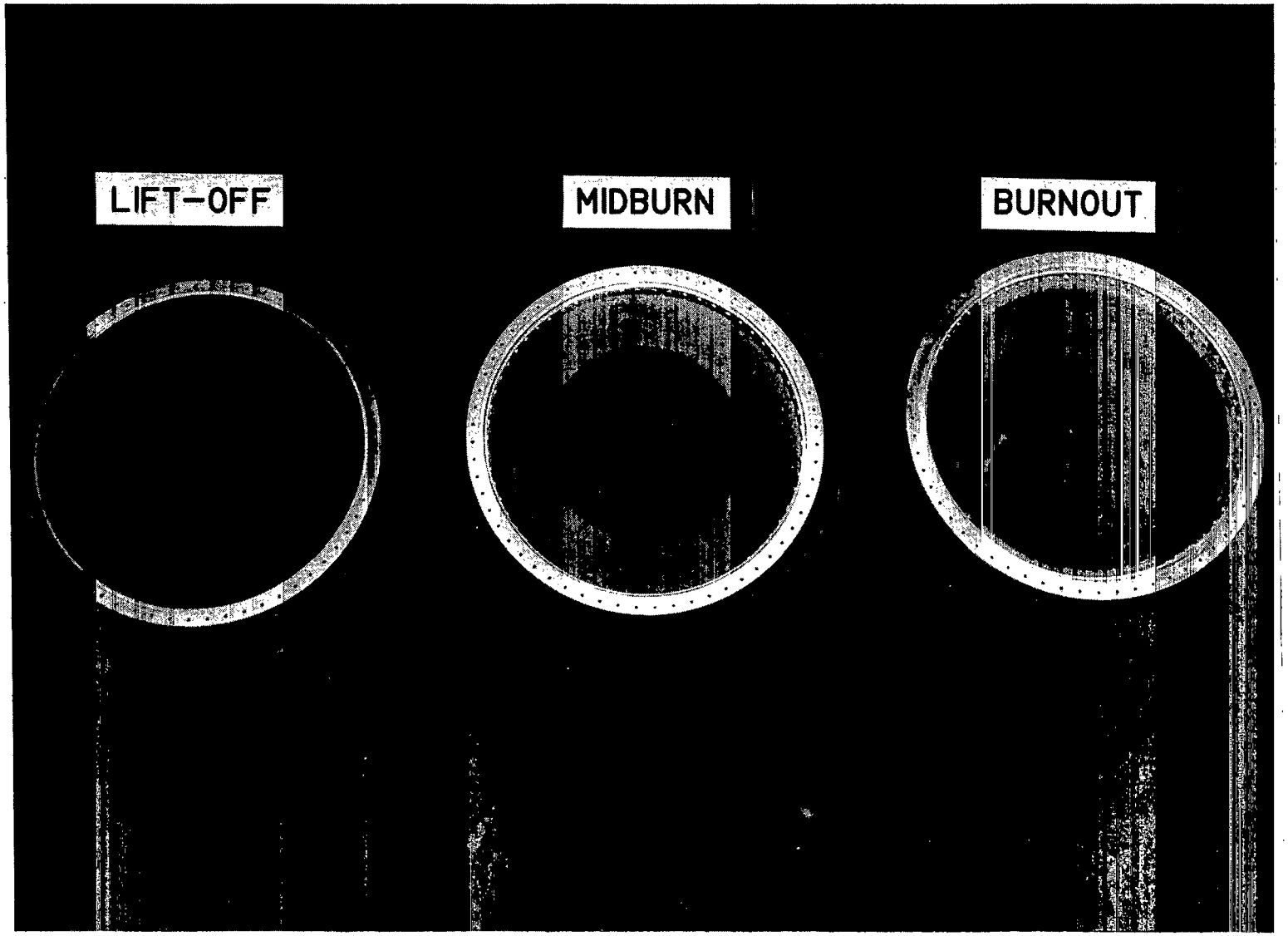

L-76-156

Figure 3.- Propellant cylinders of the 1/8-scale SRB model for different flight conditions.

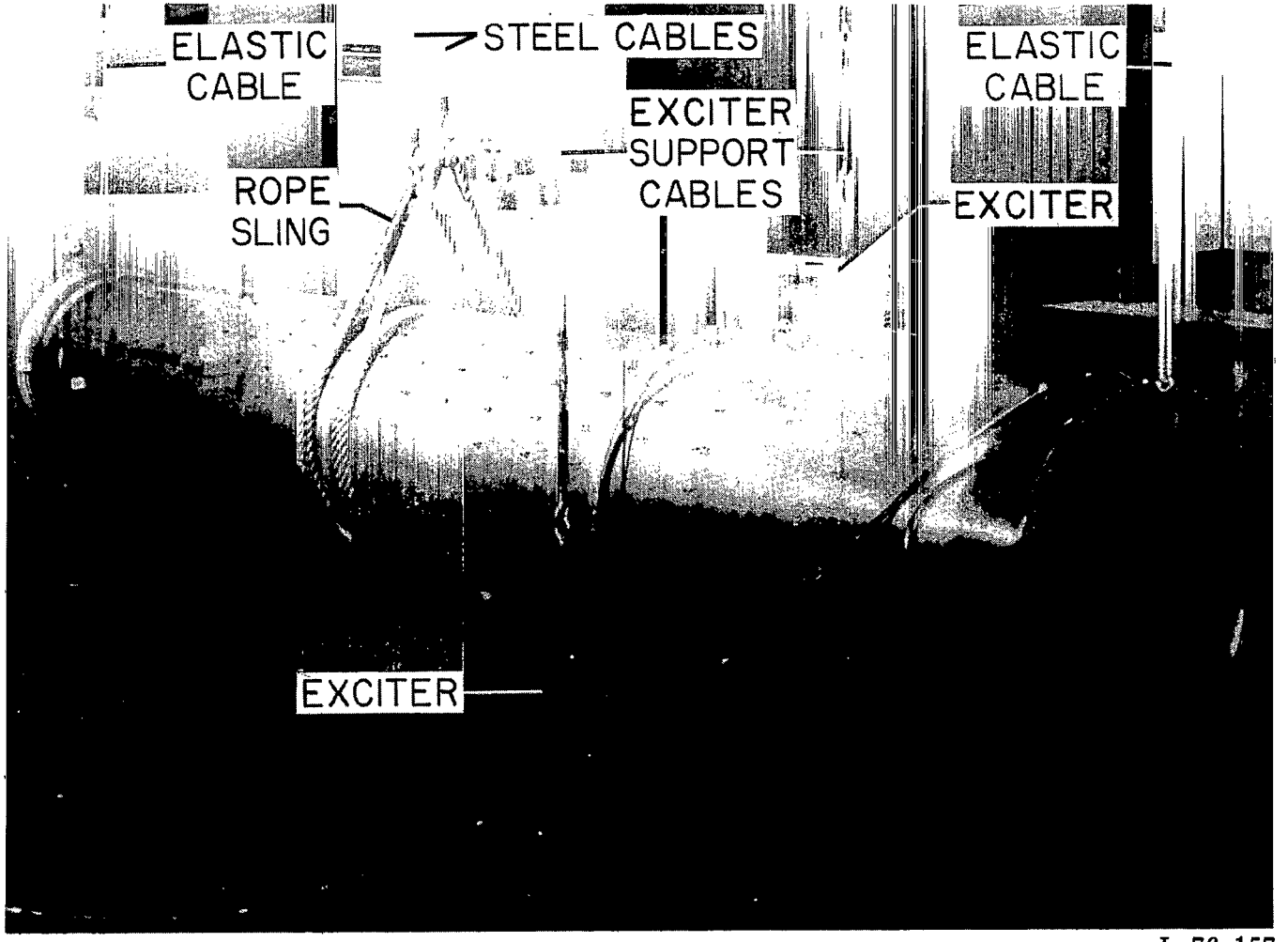

L-76-157

Figure 4.- The 1/8-scale propellant cylinder suspended for testing at midburn flight condition.

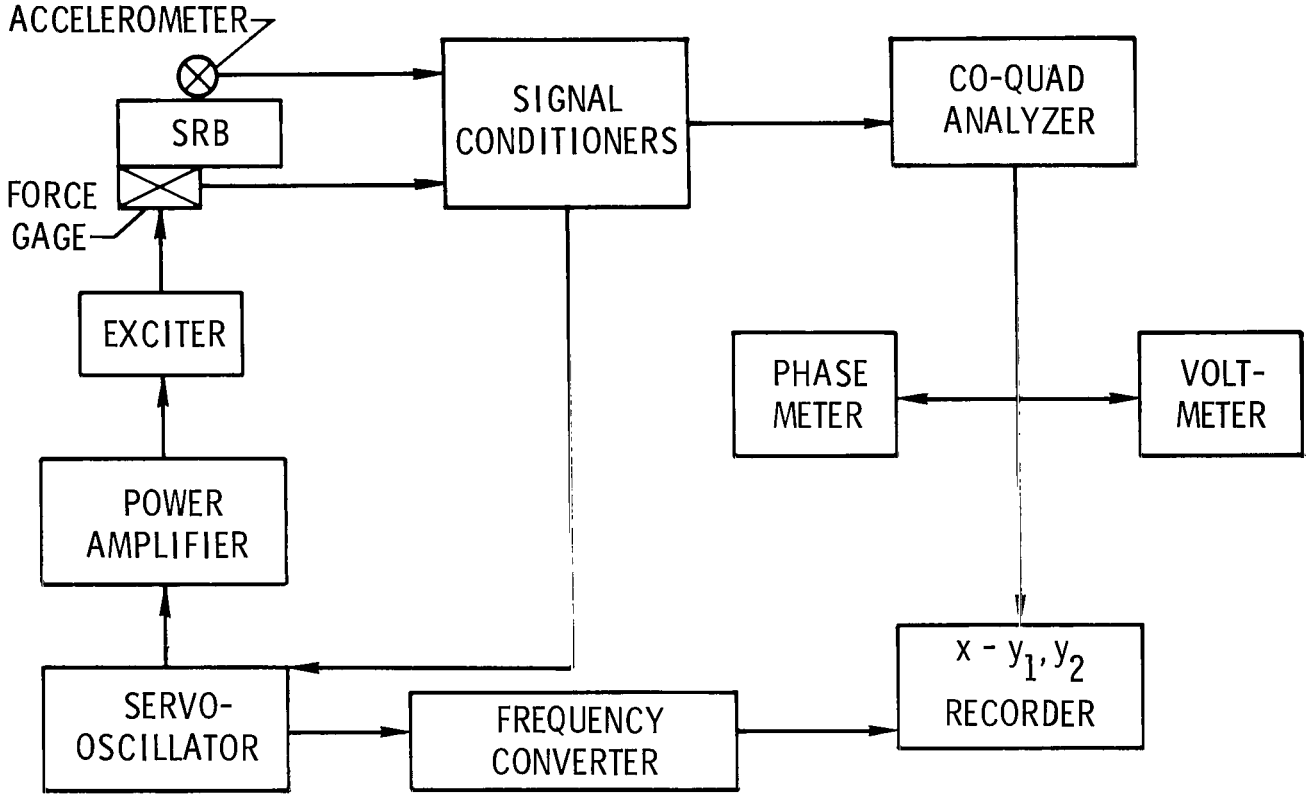

Figure 5.- Schematic diagram of data-acquisition system.

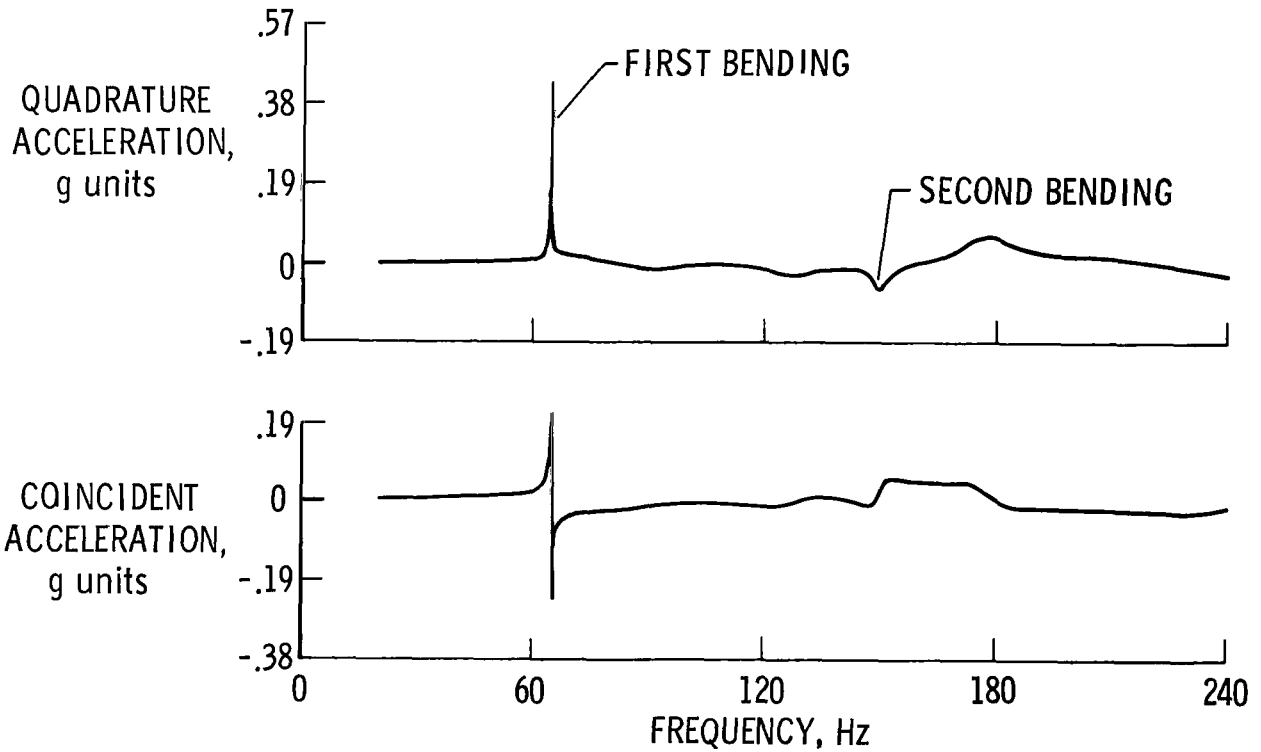

Figure 6.- Typical SRB model co-quad data with simulated free-free support for the midburn flight condition. Components are referenced to a constant servo-controlled force input of 13 N.

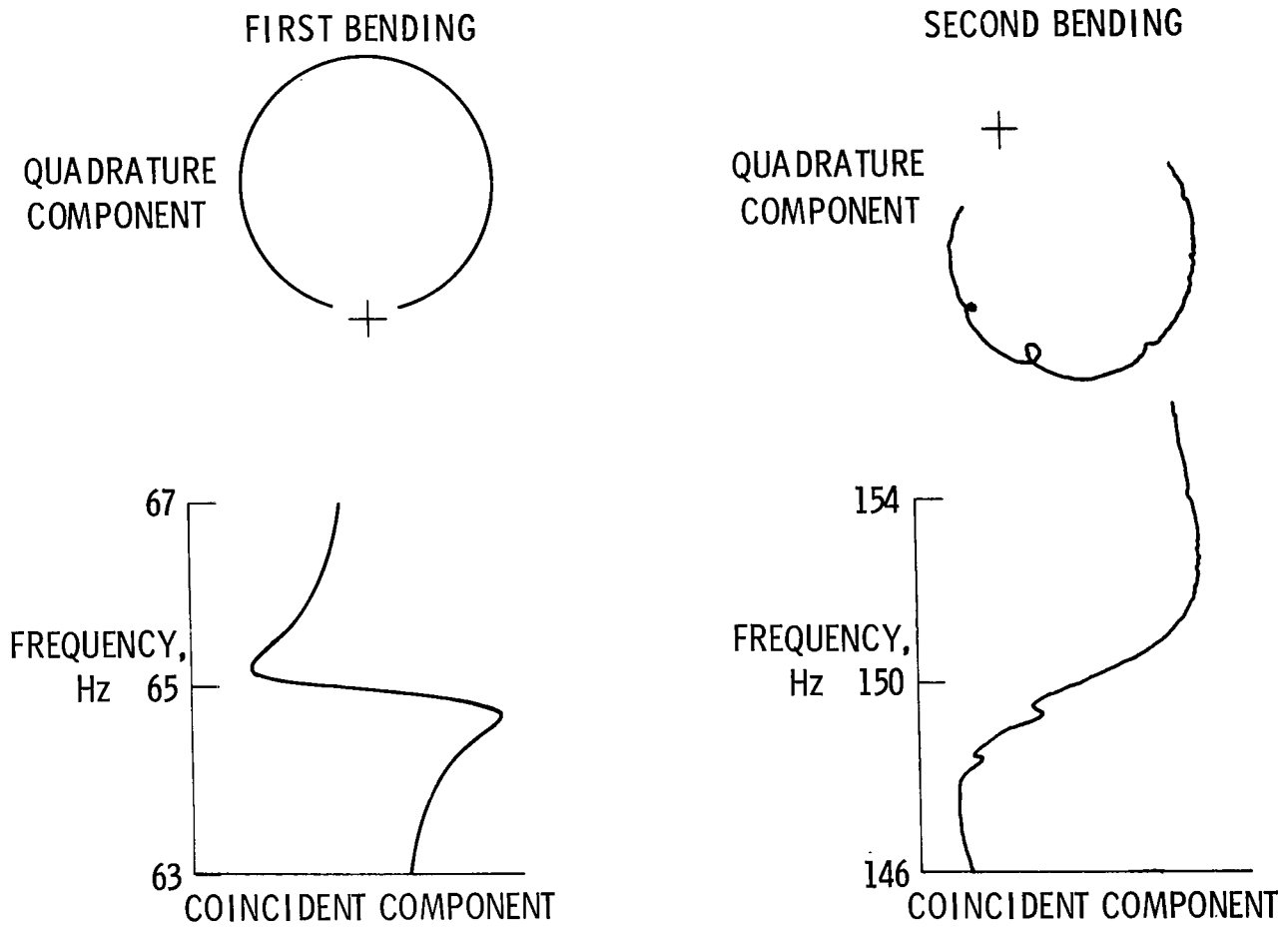

Figure 7.- Typical SRB model phase-plane (Kennedy-Pancu) data with simulated free-free support for the midburn flight condition. Components are referenced to a constant servo-controlled force input of 13 N.

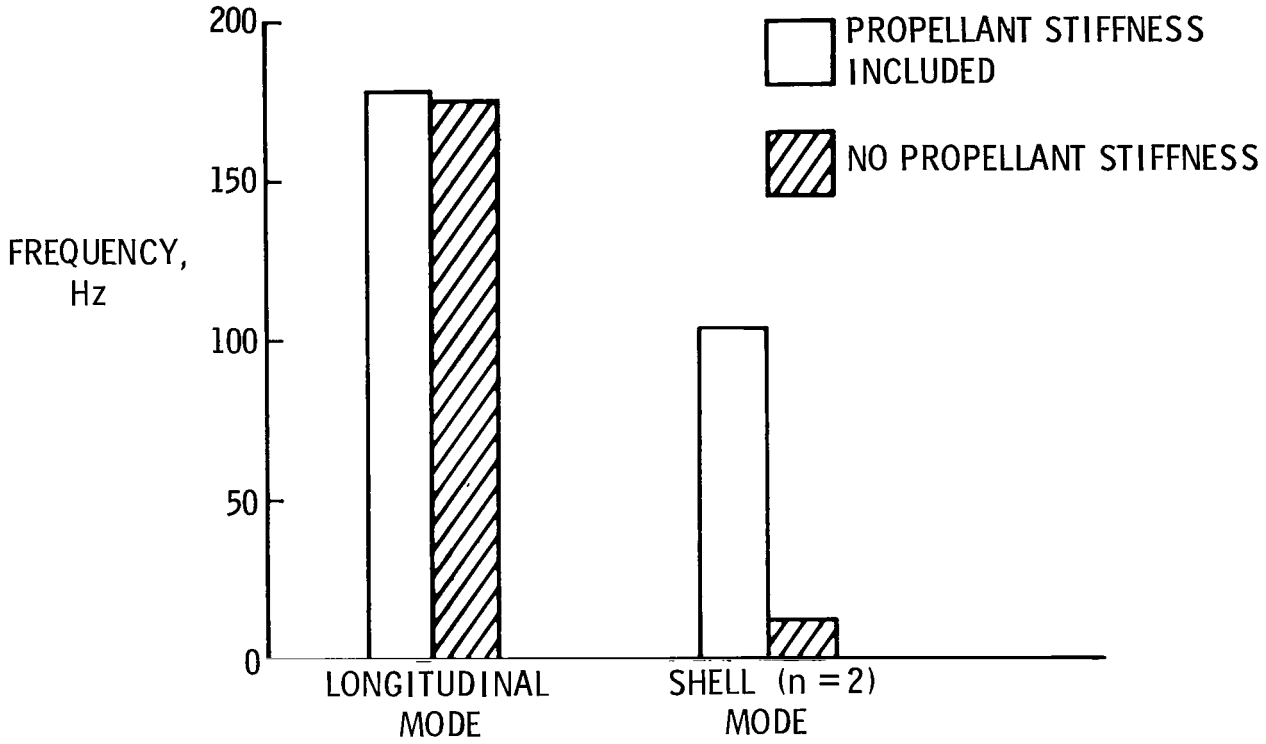

Figure 8.- Effect of propellant membrane and bending stiffnesses on frequency at lift-off flight condition.

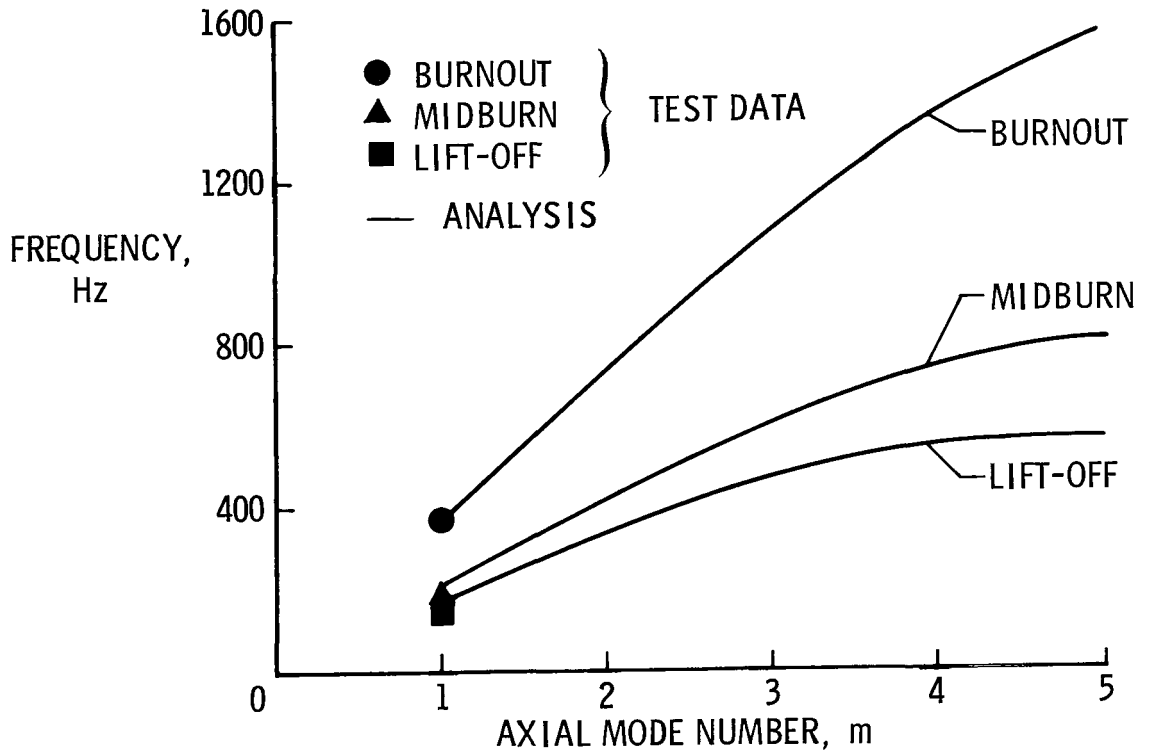

Figure 9.- Comparison of the experimental free-free longitudinal (n = 0) vibration frequencies of the 1/8-scale-model propellant cylinders with the shell-of-revolution analysis.

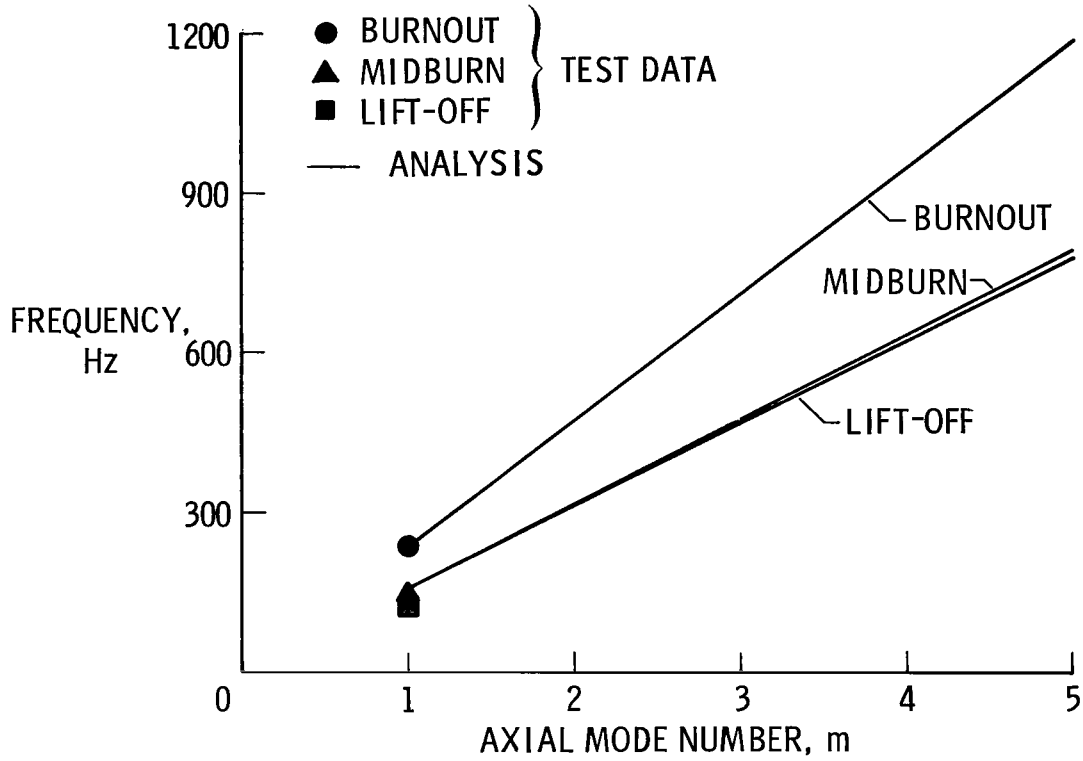

Figure 10.- Comparison of the experimental free-free torsional (n = 0) vibration frequencies of the 1/8-scale-model propellant cylinders with the shell-of-revolution analysis.

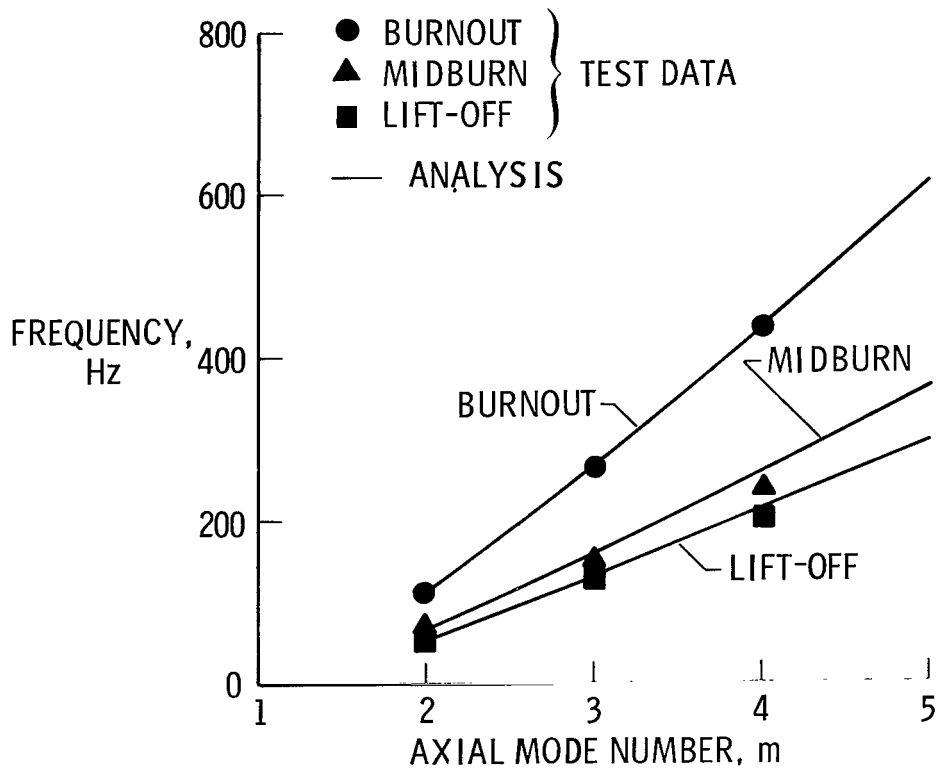

Figure 11.- Comparison of the experimental free-free bending (n = 1) vibration frequencies of the 1/8-scale-model propellant cylinder with the shell-of-revolution analysis.

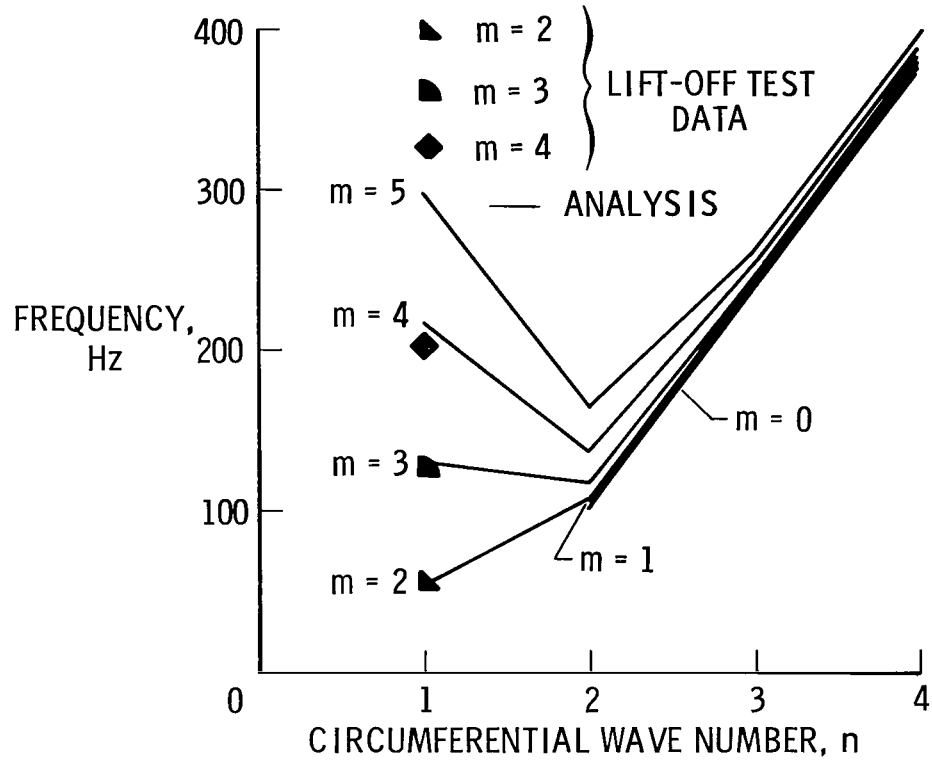

Figure 12.- Comparison of the experimental free-free shell vibration frequencies at lift-off of the 1/8-scale-model propellant cylinder with the shell-of-revolution analysis.

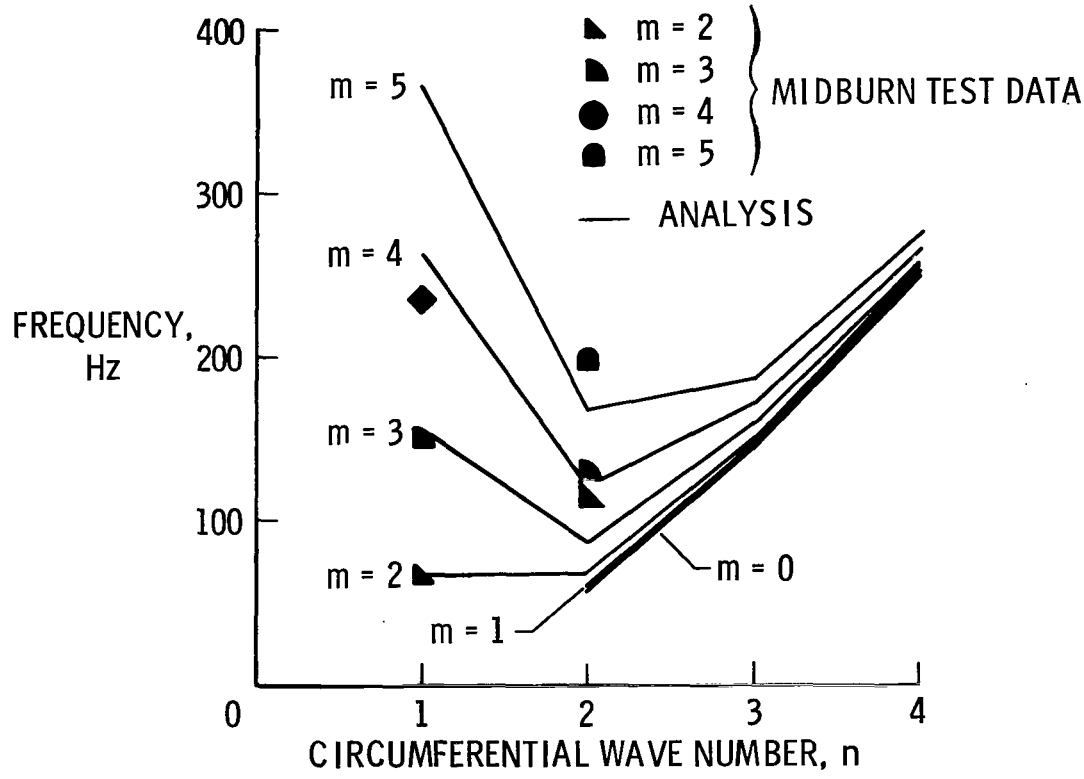

Figure 13.- Comparison of the experimental free-free shell vibration frequencies at midburn of the 1/8-scale-model propellant cylinder with the shell-of-revolution analysis.

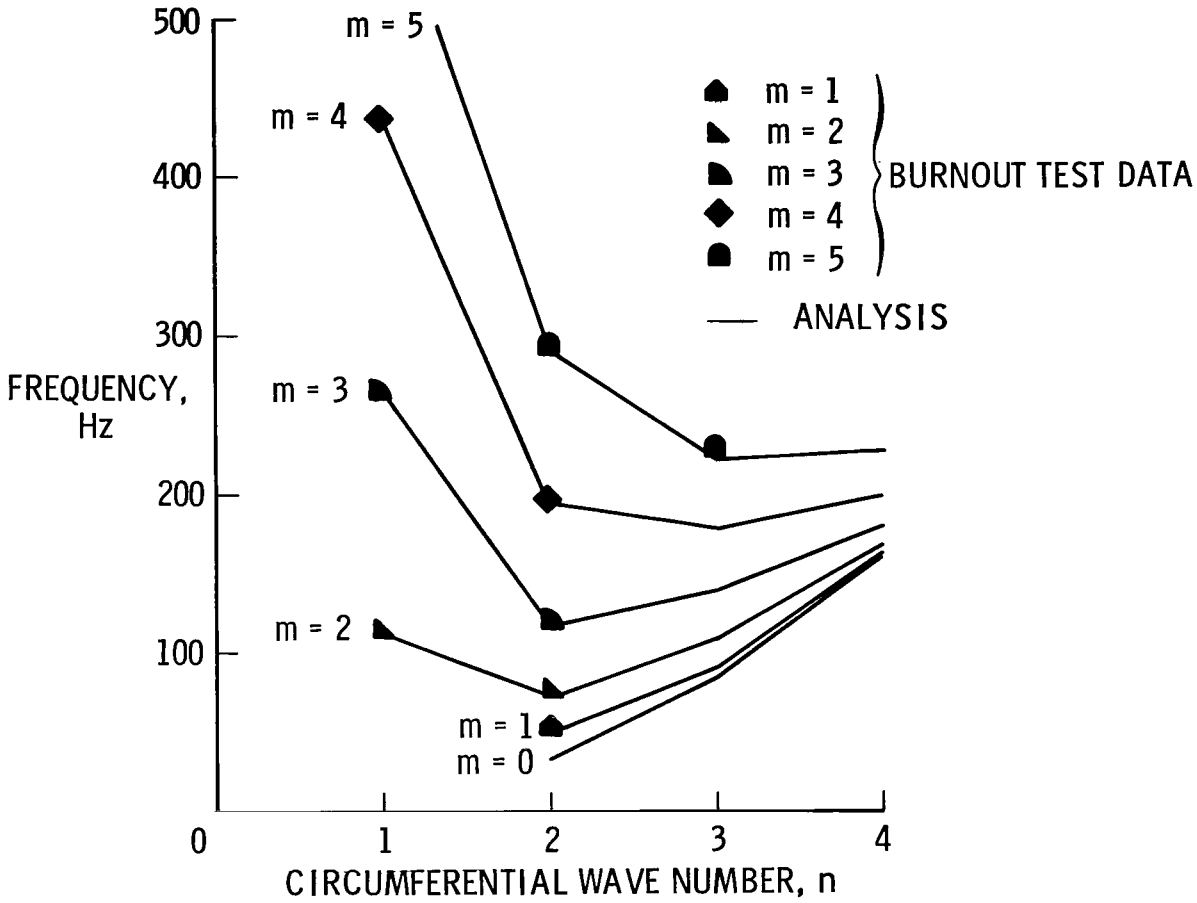

Figure 14.- Comparison of the experimental free-free shell vibration frequencies at burnout of the 1/8-scale-model propellant cylinder with the shell-of-revolution analysis.

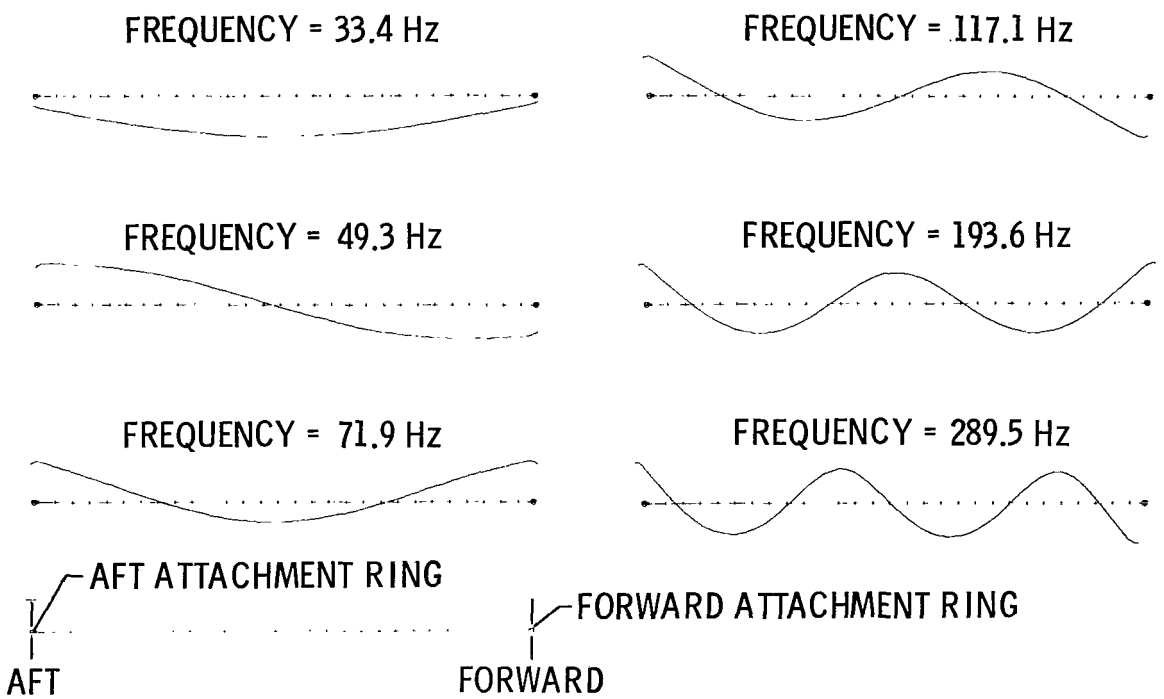

Figure 15.- Mode shapes and frequencies for normal displacement of the 1/8-scale SRB at burnout along a meridian using SOR analysis with n = 2.

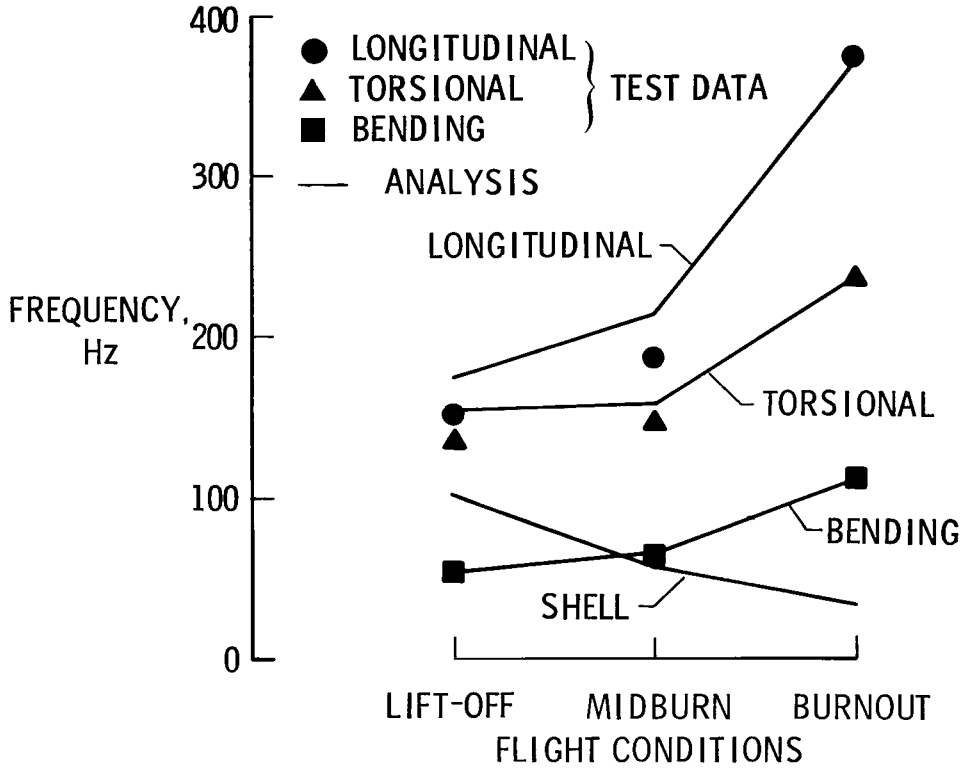

Figure 16.- First membrane, bending, and shell frequencies for the 1/8-scale propellant cylinders at different flight conditions.

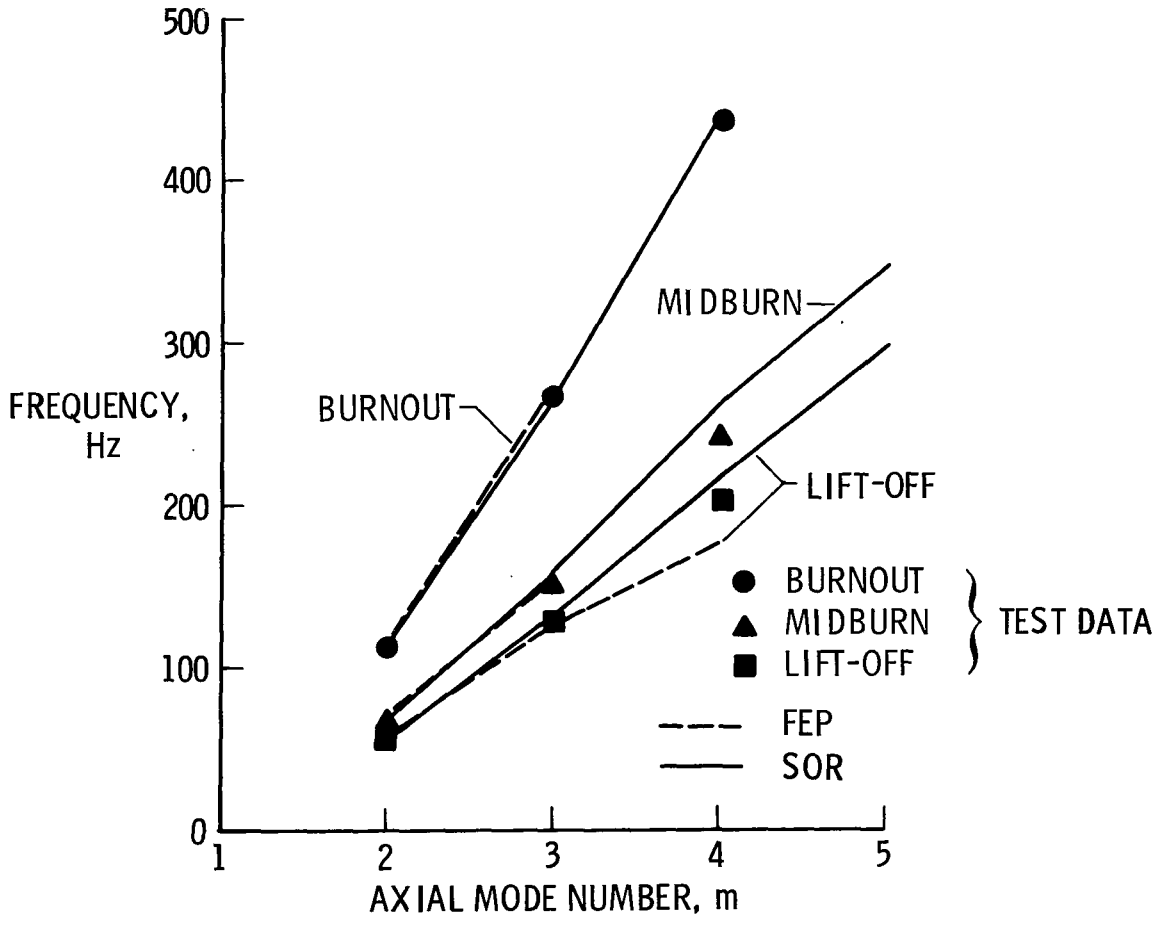

Figure 17.- Comparison of FEP and SOR model bending (n = 1) frequencies with experiment for the 1/8-scale propellant cylinders.

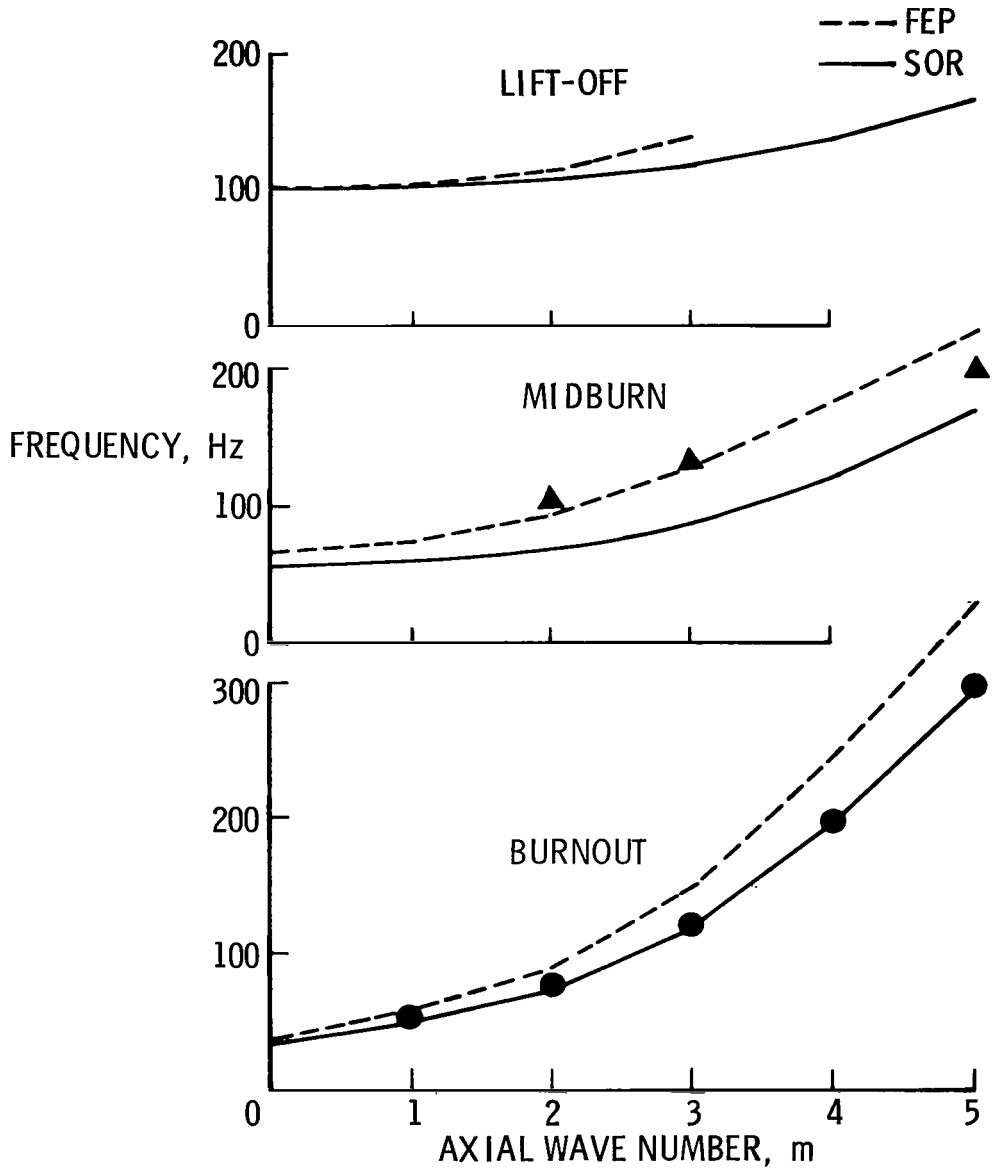

Figure 18.- Comparison of FEP and SOR models with experimental data for the 1/8-scale SRB propellant cylinders at n = 2.

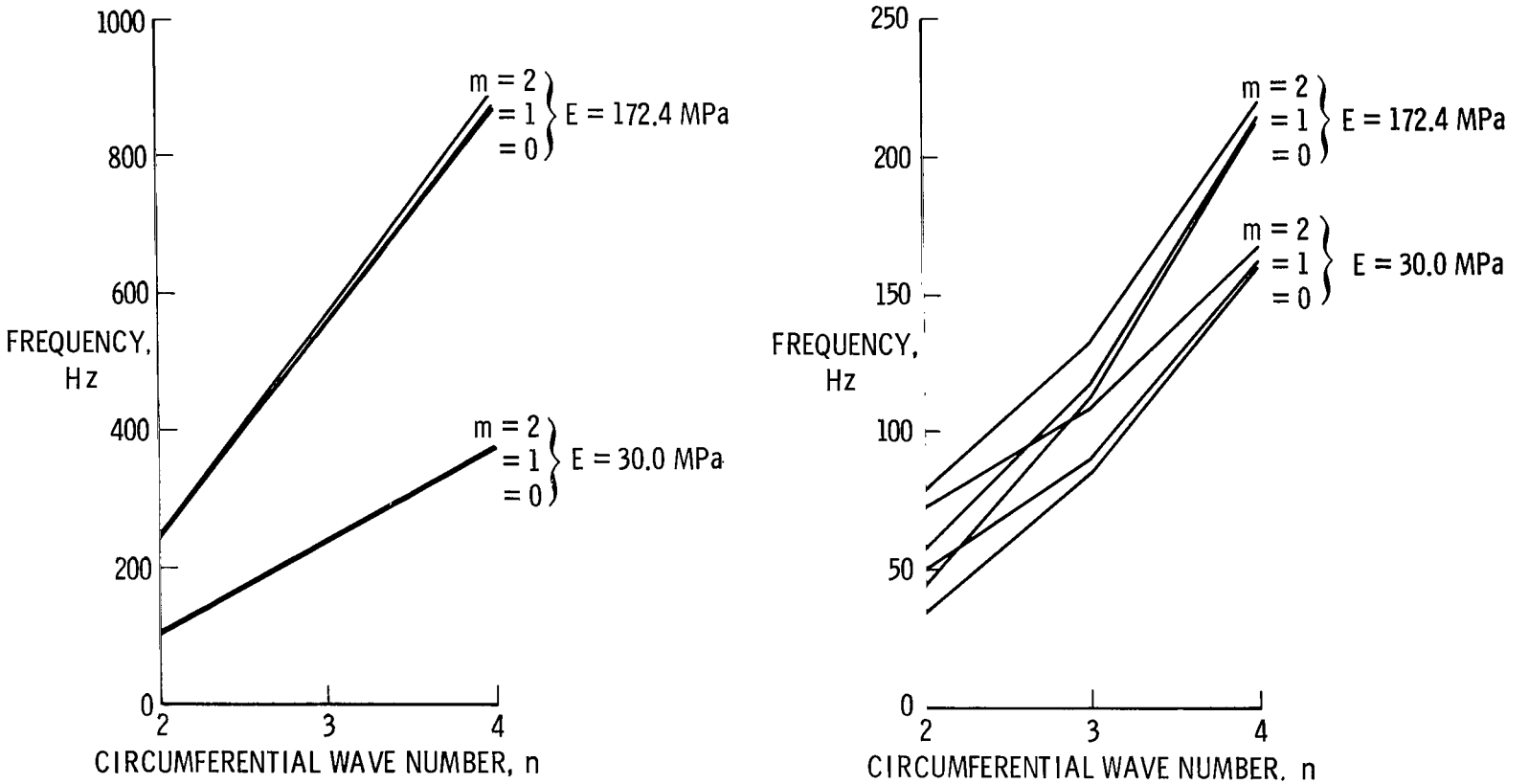

(a) Lift-off.

(b) Burnout.

Figure 19.- Variation of frequency with changes in the elastic modulus of the propellant using the SOR analysis.

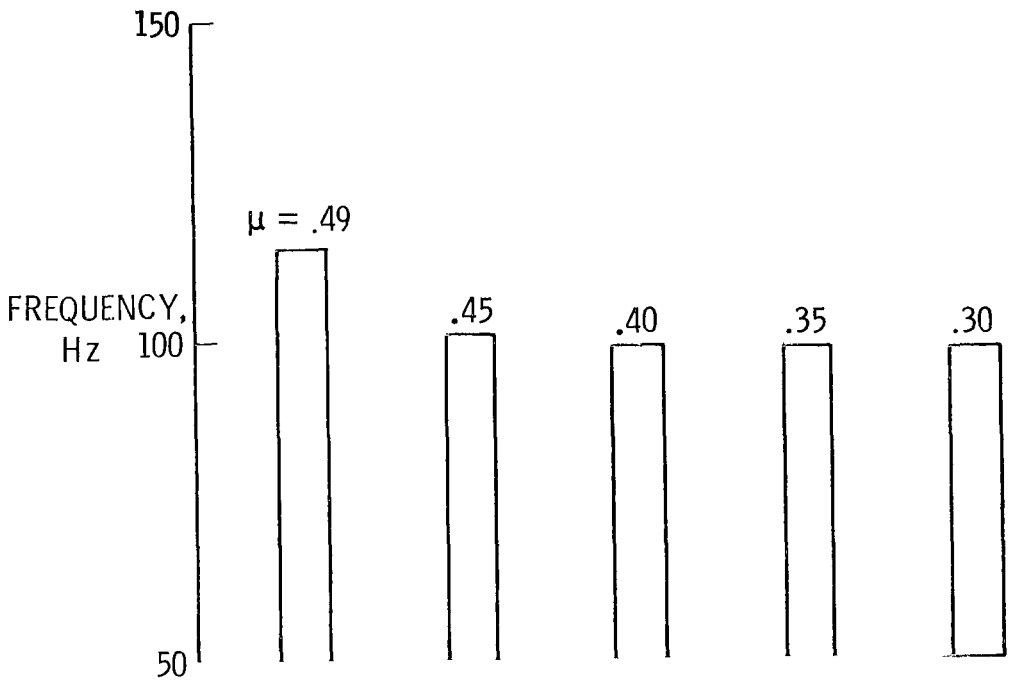

Figure 20.- Effect of varying Poisson's ratio for propellant layer on first shell frequency at $n = 2$ for lift-off flight condition. $E_p = 172.4$ MPa.

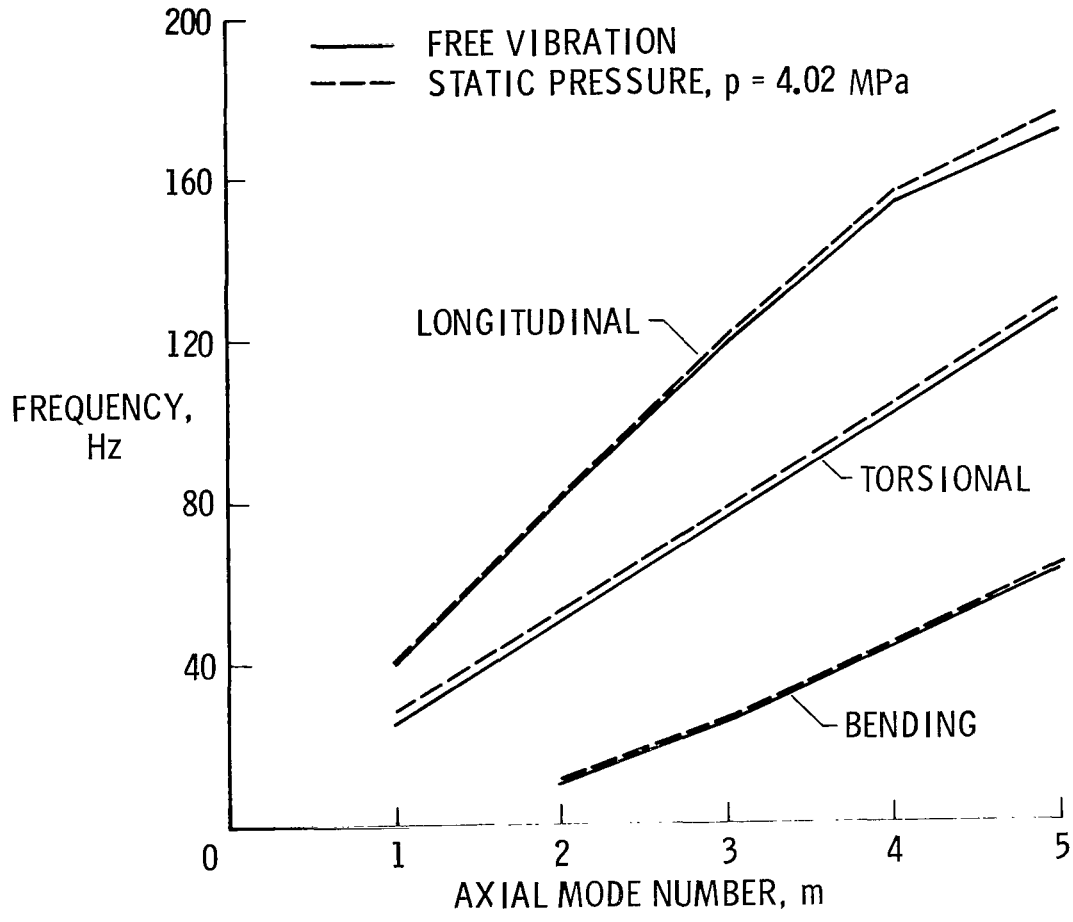

Figure 21.- Frequencies of full-scale SRB at burnout flight condition with and without an internal pressure.

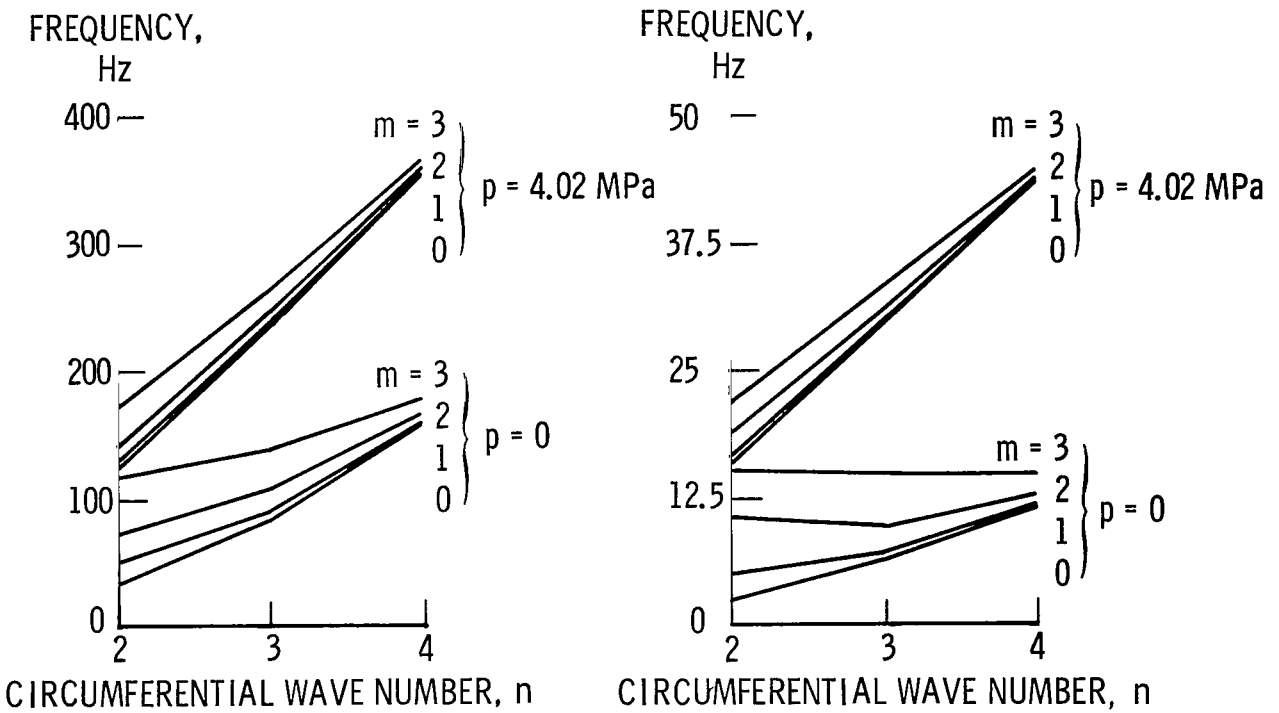

(a) The 1/8-scale SRB.

(b) Full-scale SRB.

Figure 22.- Comparison of shell-mode frequencies for 1/8-scale-model and full-scale-model propellant cylinders at the burnout flight condition with and without static internal pressure.

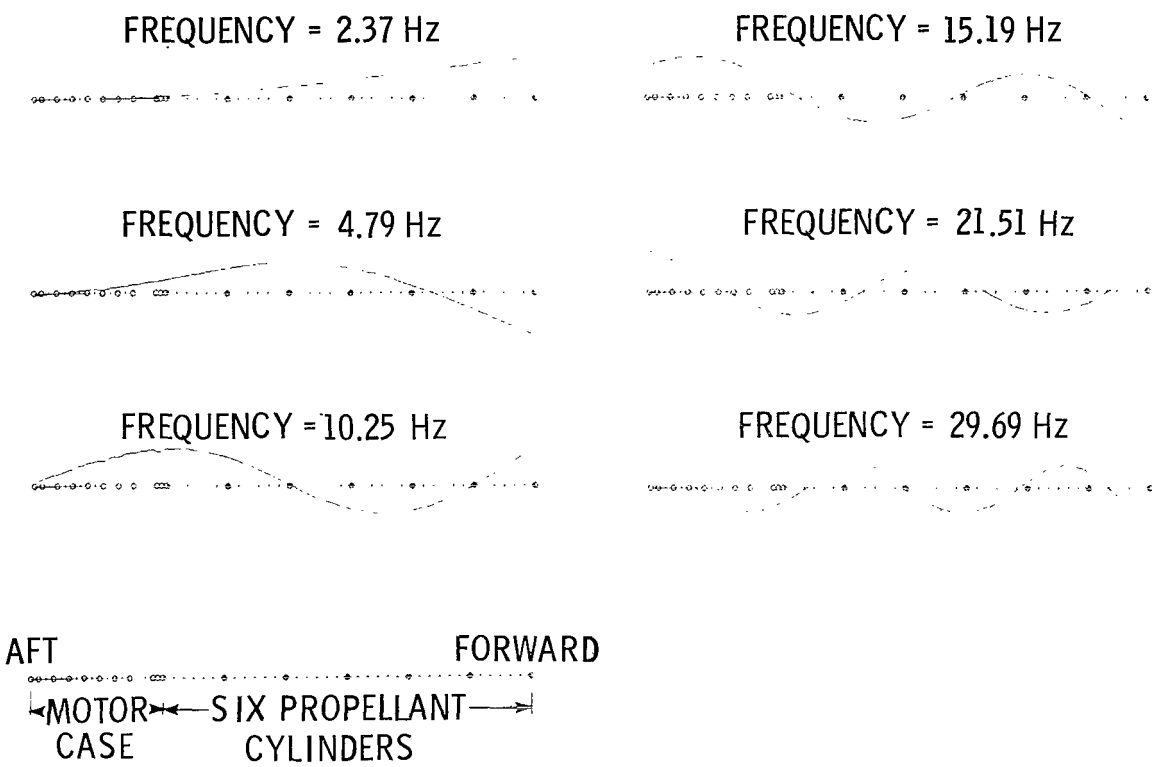

Figure 23.- Typical normal-displacement mode shapes and frequencies of full-scale SRB at burnout along a meridian using SOR analysis for n = 2.

NATIONAL AERONAUTICS AND SPACE ADMINISTRATION
WASHINGTON, D.C. 20546

OFFICIAL BUSINESS
PENALTY FOR PRIVATE USE $300

SPECIAL FOURTH-CLASS RATE
BOOK

POSTAGE AND FEES PAID
NATIONAL AERONAUTICS AND
SPACE ADMINISTRATION
451

U.S.MAIL

469 001 C1 U D 760416 S00903DS
DEPT OF THE AIR FORCE
AF WEAPONS LABORATORY
ATTN: TECHNICAL LIBRARY (SUL)
KIRTLAND AFB NM 87117

POSTMASTER: If Undeliverable (Section 158 Postal Manual) Do Not Return

"The aeronautical and space activities of the United States shall be conducted so as to contribute . . . to the expansion of human knowledge of phenomena in the atmosphere and space. The Administration shall provide for the widest practicable and appropriate dissemination of information concerning its activities and the results thereof."

—NATIONAL AERONAUTICS AND SPACE ACT OF 1958

NASA SCIENTIFIC AND TECHNICAL PUBLICATIONS

TECHNICAL REPORTS: Scientific and technical information considered important, complete, and a lasting contribution to existing knowledge.

TECHNICAL NOTES: Information less broad in scope but nevertheless of importance as a contribution to existing knowledge.

TECHNICAL MEMORANDUMS: Information receiving limited distribution because of preliminary data, security classification, or other reasons. Also includes conference proceedings with either limited or unlimited distribution.

CONTRACTOR REPORTS: Scientific and technical information generated under a NASA contract or grant and considered an important contribution to existing knowledge.

TECHNICAL TRANSLATIONS: Information published in a foreign language considered to merit NASA distribution in English.

SPECIAL PUBLICATIONS: Information derived from or of value to NASA activities. Publications include final reports of major projects, monographs, data compilations, handbooks, sourcebooks, and special bibliographies.

TECHNOLOGY UTILIZATION PUBLICATIONS: Information on technology used by NASA that may be of particular interest in commercial and other non-aerospace applications. Publications include Tech Briefs, Technology Utilization Reports and Technology Surveys.

Details on the availability of these publications may be obtained from:

SCIENTIFIC AND TECHNICAL INFORMATION OFFICE

NATIONAL AERONAUTICS AND SPACE ADMINISTRATION

Washington, D.C. 20546